

A Systematic Review of Low-Rank and Local Low-Rank Matrix Approximation in Big Data Medical Imaging

Sisipho Hamlomo^{1,2*}, Marcellin Atemkeng^{1*}, Yusuf Brima³, Chuneeta Nunhokee^{4,5,6} and Jeremy Baxter²

¹Department of Mathematics, Rhodes University, PO Box 94, Makhanda, 6140, South Africa.

²Department of Statistics, Rhodes University, PO Box 94, Makhanda, 6140, South Africa.

³Computer Vision, Institute of Cognitive Science, Osnabrück University, Wachsbleiche 27, Osnabrück, D-49090, Germany.

⁴International Centre for Radio Astronomy Research (ICRAR), Curtin University, Bentley, WA, Australia.

⁵ARC Centre of Excellence for All Sky Astrophysics in 3 Dimensions (ASTRO 3D), Bentley, Australia.

⁶Curtin Institute of Radio Astronomy, GPO Box U1987, Perth, WA 6845, Australia.

*Correspondence: sisipho.hamlomo@gmail.com, m.atemkeng@gmail.com.

Abstract

The large volume and complexity of medical imaging datasets are bottlenecks for storage, transmission, and processing. To tackle these challenges, the application of low-rank matrix approximation (LRMA) and its derivative, local LRMA (LLRMA) has demonstrated potential. A detailed analysis of the literature identifies LRMA and LLRMA methods applied to various imaging modalities, and the challenges and limitations associated with existing LRMA and LLRMA methods are addressed. We note a significant shift towards a preference for LLRMA in the medical imaging field since 2015, demonstrating its potential and effectiveness in capturing complex structures in medical data compared to LRMA. Acknowledging the limitations of shallow similarity methods used with LLRMA, we suggest advanced semantic image segmentation for similarity measure, explaining in detail how it can measure similar patches and their feasibility.

We note that LRMA and LLRMA are mainly applied to unstructured medical data, and we propose extending their application to different medical data types, including structured and semi-structured. This paper also discusses how LRMA and LLRMA can be applied to regular data with missing entries and the impact of inaccuracies in predicting missing values and their effects. We discuss the impact of patch size and propose the use of random search (RS) to determine the optimal patch size. To enhance feasibility, a hybrid approach using Bayesian optimization and RS is proposed, which could improve the application of LRMA and LLRMA in medical imaging.

Keywords: Medical imaging, Local low-rank matrix approximation, Semantic segmentation, Similarity measures, Random search, Bayesian optimization

1 Introduction

Medical images obtained using technologies such as PET, CT scans, MRI and ultrasound are crucial for diagnosing and monitoring health conditions [1–3]. These images are central to treatment planning, guiding surgical procedures, and facilitating minimally invasive procedures [4, 5]. They also play a crucial role in monitoring disease progression, evaluating treatment effectiveness and adjusting the treatment plan promptly [2, 6–8]. Rapid and accurate diagnosis through medical imaging is essential in emergency medicine to identify critical conditions and initiate urgent action [9, 10]. In addition to clinical applications, medical images contribute significantly to research, education and the emerging field of personalized medicine, where tailored treatments based on individual anatomy and pathology are becoming increasingly important [11–13]. However, handling medical data is challenging due to noise, high-dimensional data, corrupted or incomplete data, and large amounts of data that increase memory and computational time [14–18]. Various techniques have been proposed in the literature to overcome these challenges. These techniques include smoothing algorithms (i.e., Weiner filter, Gaussian filter, average filter, median filter, etc.) used in processing and analyzing medical datasets to reduce noise [19–25]. Methods such as sparse coding [26–29], discrete cosine transform (DCT) and wavelet transform are used for image compression [30–33]. In addition, techniques such as t-distributed stochastic neighbour embedding (t-SNE) and local linear embedding (LLE) are used to reduce the dimensions of these datasets [34–37]. A common limitation of the above smoothing algorithms is their limited ability to effectively handle images corrupted by complex noise patterns or non-Gaussian noise. These filters may have difficulty preserving fine details and edges in different types of noise, resulting in either over-smoothing or incomplete noise removal [38–41]. Furthermore, the DCT and wavelet transform techniques lead to blocking and ringing artefacts and are also unable to capture directional information [42, 43] while sparse coding can be computationally expensive, especially for large images [44, 45]. The computational

and space complexity of t-SNE grows quadratically with the number of data pairs, limiting its application to large datasets [46–48]. Finding an appropriate k -nearest neighbors value for all input data in LLE is challenging due to the complexity, nonlinearity, and variety of high-dimensional input data [49–51].

low-rank matrix approximation (LRMA) has shown potential in overcoming the challenges mentioned above [52–55]. LRMA refers to a technique used to approximate a given matrix as the product of two lower-dimensional matrices, to reduce the complexity of the original matrix while preserving important features. LRMA techniques allow these large datasets to be compressed and efficiently represented, enabling faster storage, transmission and processing [56–58]. However, these datasets can be affected by missing or corrupted entries due to factors such as equipment limitations or patient movement [59–61]. LRMA techniques, such as image inpainting, are used to reconstruct missing or corrupted regions of the medical images [62–64]. In signal processing, such as biological signal analysis from physiological measurements, LRMA techniques help with denoising and feature extraction to improve diagnostic accuracy [65, 66]. Genomics and proteomics use LRMA for data analysis by facilitating dimensionality reduction and pattern recognition in complex biological datasets [67, 68]. In chemoinformatics, LRMA is used in the analysis of chemical and biological data matrices in drug discovery, helping to identify relationships between molecular structures and biological activities [69, 70]. In multi-modal data fusion, that is, when dealing with data from multiple sources (e.g., imaging, clinical, genomic), LRMA is used to integrate and fuse different modalities, providing a comprehensive view for diagnosis and treatment planning [71–73].

While LRMA proves to be a valuable tool in medical imaging, it has limitations. One of the primary concerns is the potential loss of image detail and fidelity [74–76]. As the rank of the approximation decreases, fine textures, intricate patterns, and subtle color variations may be compromised, leading to a degraded image. The choice of the appropriate rank becomes crucial, striking a balance between reducing storage requirements and preserving visual quality [77, 78]. Another challenge lies in the computation time associated with LRMA methods. Singular value decomposition (SVD), a common technique for LRMA, has a time complexity of approximately $\mathcal{O}(mn \min\{m, n\})$ [79–84], where m and n are the dimensions of the image and truncating it to r singular values and vectors results in a complexity of $\mathcal{O}(mnr)$ [81–85]. This can be computationally expensive for high-dimensional images. While randomized SVD offers a faster alternative with a time complexity of $\mathcal{O}(mn \log(r))$ for rank- r approximation [84], the computation still demands careful consideration, especially for real-time applications.

The local low-rank matrix approximation (LLRMA), which is an extension of LRMA proposed in [86] in 2013 overcomes the drawbacks mentioned above and significantly relaxes the low-rank assumption. That is, instead of assuming that a matrix has a low-rank globally, they assumed that it acts

as a low-rank matrix in the neighborhood of particular row-column combinations. This approach can capture complicated spatial patterns in the data. By decomposing the input image into low-rank components specific to local regions, this technique captures local variations and fine-grained details that may be missed in global LRMA [86, 87]. This makes it particularly suitable for image processing tasks, where objects and features often have varying degrees of complexity and structure within different regions [88]. By exploiting the redundancy and similarity of neighboring regions, this technique reduces the computational complexity associated with traditional LRMA [86, 89]. This efficiency can result in faster processing times and reduced memory requirements, making it feasible to handle larger datasets and real-time applications to be processed [90].

However, LLRMA technique has its drawbacks. One notable limitation is the potential for patch artifacts or inconsistencies along the boundaries of localized regions. These artifacts can arise from abrupt transitions between adjacent regions with different low-rank structures. Careful selection of patch sizes and strategies to mitigate such artifacts are essential to ensure the quality of the approximation. In addition, for certain types of data where information from distant regions plays a critical role in the overall structure, the LLRMA may have problems capturing global dependencies and long-range interactions.

This review highlights works in the literature that apply LRMA and LLRMA to medical images. To the best of our knowledge, there is no systematic literature review that addresses LRMA and/or LLRMA with a specific focus on medical data. Due to this gap in the literature, review questions are formulated to guide the systematic investigation and evaluation. These questions help structure and guide the review process to ensure that it remains focused and addresses the most important aspects of interest.

1.1 Problematic

Medical imaging faces several challenges that affect the quality and reliability of diagnostic information. Challenges such as noise, artifacts, large amounts of data, high-dimensional data, geometric deformations, and low resolution are common in various imaging modalities [91]. These challenges are particularly detrimental to image registration, a critical process in medical imaging where information from different image modalities (e.g. MRI, CT) is aligned and integrated. High noise levels and artifacts can lead to inaccuracies in the alignment process, and the large volume and complexity of medical image data make traditional registration methods computationally intensive and error-prone. Geometric deformations further complicate accurate registration, leading to suboptimal alignment and potentially misleading clinical interpretations. Various solutions have been proposed to overcome these challenges. These solutions include image denoising [92–98], image compression [99–101], image reconstruction [71, 102–105], matrix completion [106, 107], and tensor decomposition [108–111]. While these methods have proven useful in overcoming some of these challenges by reducing noise and capturing the essential

features, they are not sufficient on their own. When using the LRMA, the local variations in medical images can be overlooked, resulting in the loss of important anatomical details [87, 90]. In addition, LRMA has difficulty dealing with the large amount of data and high dimensionality of medical images, which limits its effectiveness in preserving important information [112–116]. The LLRMA technique is important in the medical domain since it overcomes these limitations by allowing for variations in rank at the local level. This is particularly relevant in medical imaging, where subtle tissue characteristics variations can be clinically significant. LLRMA enables a more accurate representation of complex medical images, improving the performance of image processing tasks like registration.

To achieve the main objective of the study, the following questions were formulated:

- To understand and critique the application of LRMA and LLRMA in medical imaging.
- Is LLRMA more effective than LRMA when applied to medical images?
- Are there specific considerations or modifications required when applying LLRMA to different modalities of medical data?
- What are the limitations of LLRMA, and under what conditions does it perform well?
- Discuss and propose how LRMA or LLRMA can be applied to several medical data types.
- Has the medical community switched to applying LLRMA rather than LRMA?
- What are the medical datasets that are used in the literature with LRMA and LLRMA
- Review and critique the similarity measurement methods used to measure similar patches in medical imaging
- What are the most commonly used similarity measure techniques in the context of LLRMA, and how do they impact the overall performance of LLRMA techniques?
- How does the choice of the local neighborhood or patch size impact the quality of the approximation, and what are the trade-offs involved?
- Propose future research directions and solutions
- Discuss the applicability and feasibility of the proposed solutions.

This investigation fills the research gaps by comparing LRMA and LLRMA applied in the medical imaging field in terms of their strengths, weaknesses and limitations and suggests the way forward in this field.

1.2 Contributions

In this study, we conducted a comprehensive review of 47 publications. Of these, 25 applied LRMA techniques to medical data and 32 applied LLRMA techniques between 2006 and 2023. We discuss various datasets that have

been used in LRMA or LLRMA applications. In addition, we summarize various tasks that have been performed on these datasets and recommend other machine-learning tasks that could be performed. We highlight a notable shift in preference for LLRMA in the medical field since 2015, demonstrating its potential and effectiveness in capturing complex structures in medical data compared to LRMA.

We acknowledge the limitations of shallow similarity methods commonly used in this field and suggest exploring advanced deep learning models such as DeepLab [117]. We explain in detail how DeepLab can measure similar patches and how feasible it is. Furthermore, our study highlights the importance of applying LRMA to different modalities of healthcare data, including structured and semi-structured data. We discuss the limitations of LRMA on irregular data types and show how LRMA can also be used on regular data with missing entries. We extend this by discussing the impact of inaccuracies in the prediction of missing values and how these affect the application of LRMA. In addition, the impact of patch size is addressed and we propose the use of a random search (RS) technique to find the optimal patch size. To improve the feasibility of this method, we propose a hybrid approach using Bayesian optimization and RS.

1.3 Manuscript Organization

The organization of this work is as follows: Section 2 discusses the methodology used in this paper. Section 3 investigates the application of LRMA to medical data and highlights various methods researchers propose to improve the quality of medical imaging datasets, such as MRI, CT, microarray, and infrared imaging. Section 4 reviews the literature on the application of LLRMA to various medical imaging modalities. Section 5 presents various medical datasets used in LRMA and LLRMA. Section 6 explores various similarity measurement algorithms used to measure similar patches. Section 8 discusses the results and drawbacks of applying the LRMA technique to medical data. Section 9 suggests possible future research directions and discusses the applicability and feasibility of the proposed solutions. This section serves as a conclusion of the research and summarizes the main findings of the study.

2 Methodology

This systematic review examines LLRMA to establish a comprehensive and rigorous approach that identifies, selects, and evaluates relevant field studies. The methodology outlines the systematic process that will be followed to ensure the review's transparency, reliability, and replicability. This process includes formulating the research question, defining inclusion and exclusion criteria, systematically searching literature databases, reviewing and selecting studies according to predefined criteria, extracting data from the selected studies and assessing the quality and potential biases in the included studies. In this study, we follow methodology based on the frameworks proposed by

[118] for systematic review. First, we define a strategy for conducting a comprehensive literature search. The defined search strategy is then executed, and publications that meet the predefined inclusion and exclusion criteria are identified. Relevant data are extracted through thorough reading and synthesis of the selected publications. In the final step, the extracted data is analyzed and interpreted to summarize the current state of research and suggest new ways for further investigation.

2.1 Data Sources and Search Strategy

In this systematic review, we used three databases, namely, Scopus, Web of Science and PubMed, to collect publications using the advanced search. Keywords were identified to compose the search string to select studies to answer the research questions. Boolean operators were used to combine and divide these strings. Publications were first selected based on their title, keywords, and abstracts. Table 1 shows the search details.

2.2 Selection and Data Extraction

The selection of studies for this systematic review followed predefined inclusion and exclusion criteria to ensure relevance and quality. Following the search mentioned in Section 2.1, all journals were imported into different Excel sheets and sorted by keywords. Duplicates were removed using the VLOOKUP and COUNTIF functions. The COUNTIF function counts the number of cells within a specified range that meet a given condition or criteria. It was used in our case to count the number of times a specific journal appeared in a sheet (i.e., checking for duplicates within the sheet). The VLOOKUP function, on the other hand, was used to look up a journal in a sheet and return a corresponding journal from another sheet in the same Excel workbook, that is, checking if a journal in Sheet1 also appears in sheet2 on the same Excel workbook. After removing duplicates, relevant studies were chosen based on the inclusion and exclusion criteria. Remaining studies were then evaluated against the inclusion criteria, any differences were discussed, and an agreement was reached. Fig. 1 depicts the study selection procedure. A standardized form was developed for data extraction, which included key aspects such as study details (i.e., title, authors, publication year), LLRMA techniques (i.e., SVD, PCA), application (i.e., image denoising, classification), main results, and conclusion. Two reviewers independently extracted data from the included studies.

2.3 Inclusion, Exclusion and Quality Assessment

The study included publications that satisfied specific inclusion criteria and underwent a quality assessment.

Table 1 Search strings used in different databases.

Database	Advanced search string	Search date	Results
Web of Science	ALL=((“low-rank approximation” OR “low-rank approximation” OR “local low-rank approximation” OR “local low-rank approximation”) AND (“image compression” OR “image filtering” OR “medical images”))	02 Sep, 2023	1097
Scopus	TITLE-ABS-KEY(((“low-rank approximation” OR (“low-rank approximation”) OR (“local low-rank approximation”) OR (“local low-rank approximation”)) AND ((“image compression”)) OR (“image filtering”)) OR (“medical images”)))	02 Sep, 2023	909
PubMed	((“low-rank approximation”)) OR (“low-rank approximation”) OR (“local low-rank approximation”) OR (“local low-rank approximation”)) AND ((“image compression”)) OR (“image filtering”)) OR (“medical images”))	02 Sep, 2023	6
Total			2012

2.3.1 Inclusion and Exclusion Criteria

The publications were collected from search engines (Scopus, Web of Science, and PubMed), and relevant studies were selected based on predefined inclusion and exclusion criteria.

- Inclusion criteria: The publications included in this systematic review met the requirement of applying matrix approximation. In addition, they met at least one of the following requirements:
 - i. In the study, a technique is used to compress or denoise or reconstruct or complete an image, etc.
 - ii. The study discusses LLRMA.
 - iii. The study applies LRMA or LLRMA on medical images.
- Exclusion criteria: Publications were excluded from this review if they met at least one of the following criteria:
 - i. The publication is not written in English.
 - ii. The publication does not discuss LRMA or LLRMA.
 - iii. The publication is a reduced version of another retrieved publication.
 - iv. The publication is not peer-reviewed.

2.3.2 Quality Assessment

The quality of all the selected publications was evaluated. To determine the research’s reliability and soundness, publications were assessed using the following checklist:

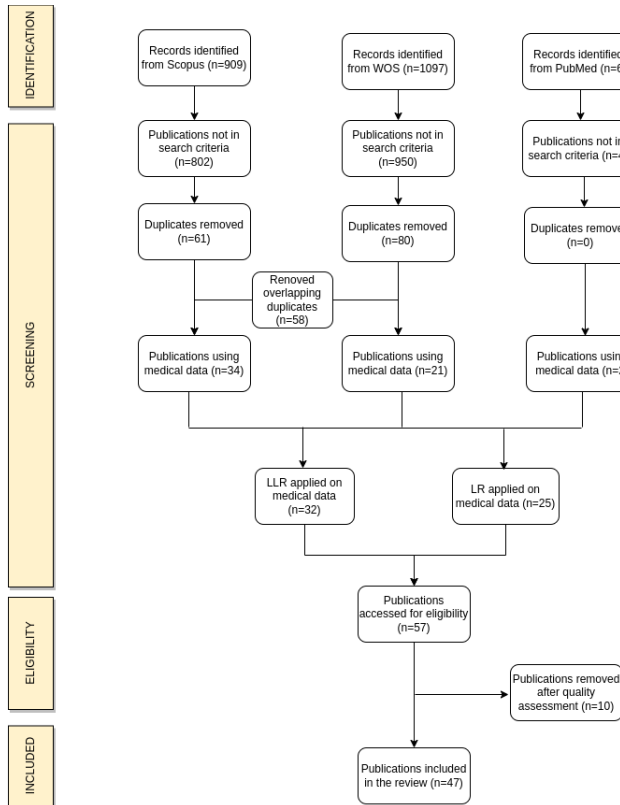


Fig. 1 Flow chart depicting the study selection process for the systematic literature review.

- Are the research objectives well-defined? Is the statistical analysis appropriate for the study's research question and objectives?
- Does the data support the conclusion? Are the study's limitations and implications discussed?
- Are references relevant, up-to-date, and correctly cited? Do other authors cite the study?

3 LRMA Applied to Medical Data

Researchers in medical imaging have proposed various methods to improve the quality of MRI, CT, microarray, and infrared imaging data. [94], for instance, proposed using SVD-based LRMA approximation to reconstruct and denoise multi-dimensional MRI data. [95], on the other hand, used SVD to compress the size of the dictionary in the time domain for pattern recognition, whereas [108] proposed a proximal operator for tensor nuclear norm approximation based on tensor-train rank-1 (TTr1) decomposition through SVD. In [98], the authors introduced low tensor-train rank and low multilinear rank approximations to concurrently address despeckling and compression in tomography

images, targeting a specified compression ratio. In addressing the calculation of optimal regularized inverse matrices subject to rank constraints, [119] proposed an effective rank-update technique that decomposes the problem into smaller rank-related challenges. In contrast, [109] proposed the use of multi-contrast Hankel tensor completion (MC-HTC) to leverage shared information in multi-contrast datasets, considering their highly correlated image structure, joint spatial support, and joint coil sensitivity for joint reconstruction. Meanwhile, in [107], an enhanced fixed-rank approximation algorithm (IFRAA) was proposed to address the limitations of the fixed-rank approximation algorithm (FRAA) when estimating missing values in a gene expression matrix.

[103] proposed a method to improve the quality of fast T2 mapping, while [102] proposed a reconstruction framework for magnetic resonance fingerprinting. Another area of research has been on spatiotemporal reconstruction for dynamic MRI, as seen in the works of [104] and [105]. On the other hand, [96] proposed a spatiotemporal low-rank total variation method to recover the arterial spin labelling MRI (ASL-MRI) data. Additionally, researchers have explored LRMA methods for MRF dictionaries, as discussed in [97].

In other areas of medical imaging, researchers have also proposed various techniques. For instance, [120] proposed an extension matrix CUR decomposition to tensor-based datasets with distinguished mode. [121] proposed an image-domain multi-material decomposition method for dual-energy computed tomography (DECT) that aims to suppress noise, reduce cross-contamination, and improve the accuracy of decomposed material images. Meanwhile, [106] proposed a method that factorizes an image matrix as a sum of rank-one matrices, where the rank is automatically estimated during convergence, eliminating the need for pre-specified rank information. On the other hand, [122] introduced a novel supervised descriptor learning (SDL) technique for multi-output regression that can construct discriminative and compact feature representations to improve multivariate estimate performance in medical images. The SDL algorithm extracts discriminative and compact feature representations using LRMA with supervised manifold regularization. Lastly, [71] proposed a multi-modality medical image fusion method for computer-aided diagnosis applications. The proposed method suppresses noise in medical images and provides detailed information for disease diagnosis.

These works highlight the importance of LRMA and regularization techniques in medical imaging. Table 2 gives a summary of the above-discussed publications. This table summarizes the low-rank methods applied to medical datasets with different modalities. It provides information on the strengths and weaknesses of the papers that have used low-rank methods in various applications. The table includes references, year of publication, application, low-rank method used, strengths, and weaknesses of each publication.

Table 2 Summary of low-rank method, source code, strengths and weaknesses of papers applying LRMA to medical datasets with different modalities. The term "Not provided" was used for publications where the source code was not provided and we could not find it on the authors' website or github.

References	Year	Application	Low-rank method	Source code	Strengths	Weakness	
Mahoney et al. [120]	2006	Image compression and reconstruction	SVD	Not provided	<ul style="list-style-type: none"> •Captures the most essential underlying structures and patterns in the data for compression, reconstruction, and other tasks. 	<ul style="list-style-type: none"> •May not perform well for tensors with multiple equally important modes or similar properties. 	
Friedland et al. [107]	2006	Estimating missing values	SVD	Not provided	<ul style="list-style-type: none"> •Local-global algorithm exploiting local data similarity. 	<ul style="list-style-type: none"> •Computational complexity not extensively discussed; may be computationally intensive for large-scale micro-array datasets. 	
Lyra et al. [94]	2012	Denoising images	MRI	SVD	Not provided	<ul style="list-style-type: none"> •Estimates number of singular values using AIC, not just visual inspection. 	<ul style="list-style-type: none"> •Equally compresses the dataset.
Cheng et al. [110]	2014	Tracking curvilinear structures in dynamic X-ray images.	Tensor decomposition	Not provided	<ul style="list-style-type: none"> •Uses tensor-based algorithm with model propagation for robust tracking. 	<ul style="list-style-type: none"> •Specifically designed for tracking deformable objects in X-ray images; may not apply directly to other types of images or objects. 	
Mcgivney et al. [95]	2014	Image compression	SVD	Not provided	<ul style="list-style-type: none"> •Reduces computations without sacrificing signal-to-noise. 	<ul style="list-style-type: none"> •Applies equal weight to different singular values. 	
Fang et al. [96]	2015	Image denoising	SVD	Not provided	<ul style="list-style-type: none"> •Uses joint spatial total variation and temporal low-rank regularization for improved SNR in ASL-MRI. 	<ul style="list-style-type: none"> •Due to low signal-to-noise ratio, multiple acquisitions are required, leading to a longer scan time. 	

Table 2 Cont.

References	Year	Application	Low-rank method	Source code	Strengths	Weakness
Peng et al. [103]	2016	Image reconstruction	SVD	Not provided	<ul style="list-style-type: none"> Utilizes exponential parametric model in a relaxed manner to balance the trade-off between data consistency and the exponential structure. 	<ul style="list-style-type: none"> Applies a uniform threshold to enforce Hankel low-rankness across all spatial locations.
Ulas et al. [104]	2016	Image reconstruction	Nuclear norm minimization	Not provided	<ul style="list-style-type: none"> The suggested approach utilizes a reconstruction model that integrates penalties for dTV sparsity and nuclear norm simultaneously. 	<ul style="list-style-type: none"> Nuclear norm minimization is sensitive to noise and outliers in the data.
Xu et al. [105]	2017	Reconstruction of dynamic MRI data	RPCA	Not provided	<ul style="list-style-type: none"> Employs a tighter nonconvex rank approximation, leading to improved image clarity and computational efficiency. 	<ul style="list-style-type: none"> How effective the method is in different imaging modalities is not explored.
Chung et al. [119]	2017	Optimization	SVD	https://github.com/juliannechung/ORIM	<ul style="list-style-type: none"> Breaks down the optimization issue into smaller subproblems of varying ranks and employs gradient-based techniques capable of leveraging linearity. 	<ul style="list-style-type: none"> Employing diverse noise levels in each problem or incorporating larger alterations in k_j could lead to extended CPU times and/or elevated reconstruction errors in the update approach.
Assländer et al. [102]	2018	Reconstruction accuracy noise propagation	SVD	https://bitbucket.org/asslaender/nyu_mrf_recon/src/master/	<ul style="list-style-type: none"> The LRMA approximation simplifies the computation by reducing the need for numerous Fourier transformations in the signal evolution. 	<ul style="list-style-type: none"> The limitations and effectiveness of the proposed method in different imaging modalities are not explored.
Yang et al. [97]	2018	Image compression	Randomized SVD	Not provided	<ul style="list-style-type: none"> Decreases the memory needed to produce high-resolution MRF maps and enhances the overall speed of the compression process. 	<ul style="list-style-type: none"> Randomized SVD may perform differently based on the specific properties of the MR fingerprinting matrix.

Table 2 Cont.

References	Year	Application	Low-rank method	Source code	Strengths	Weakness
Ding et al. [121]	2018	Image-domain multi-material decomposition for dual-energy CT	SVD	Not provided	<ul style="list-style-type: none"> Enhances image resolution and accuracy through noise suppression and reduced cross-contamination. 	<ul style="list-style-type: none"> Equal weighting to singular values in SVD.
Liu et al. [108]	2020	Tensor completion	SVD	Not provided	<ul style="list-style-type: none"> Utilizes tensor train rank-1 (TTr1) decomposition, enhancing decomposition accuracy. 	<ul style="list-style-type: none"> Incorporates total variation as regularization, potentially unsuitable for datasets without significant local smoothness.
Li et al. [106]	2020	Matrix completion	l_p -norm minimization	Not provided	<ul style="list-style-type: none"> Robust to outliers, no need for rank or noise information. 	<ul style="list-style-type: none"> Uniform weighting of singular values in l_p-norm minimization.
Yi et al. [109]	2021	Image reconstruction	HOSVD	https://github.com/loyalliu/MC-HTC	<ul style="list-style-type: none"> Enables tensor low-rankness via higher-order SVD, improving reconstruction of multiple slices. 	<ul style="list-style-type: none"> Iterative updates and higher-order SVD increase computational complexity.
He et al. [71]	2022	Reconstruction and image fusion	SVD	https://github.com/VCMHE/FDO_DPGF	<ul style="list-style-type: none"> Utilizes rank coefficient optimization of LLRMA for multi-modality medical image reconstruction. 	<ul style="list-style-type: none"> Equal weight application to different singular values in SVD.
Kopriva et al. [98]	2023	Despeckling and compression	Tensor SVD	https://github.com/ashkan-abbas166/NWSR	<ul style="list-style-type: none"> Simultaneously suppresses speckle and provides memory-efficient low-dimensional representations. 	<ul style="list-style-type: none"> Evaluation on a limited dataset may not fully represent OCT image diversity in various clinical scenarios.

4 LLRMA Applied to Medical Data

LLRMA is a technique that is applied to medical data to effectively analyze and extract meaningful information while reducing computational complexity and noise. The term *local low-rank* refers to finding low-rank sub-matrices within localized regions or areas of the data. Medical data often exhibit spatial or temporal correlations where neighbouring regions exhibit similar patterns or structures. By applying LLRMA methods, we can exploit these local correlations and represent the data in each partial region where the rank of each of the small partial regions is smaller than that of the entire data. This enables more efficient processing and analysis of medical data, especially in scenarios with high-dimensional data. Applying LLRMA to medical data provides a robust framework for processing high-dimensional, spatially or temporally correlated data. By exploiting the inherent structure and redundancy within localized regions, efficient processing, noise reduction, dimensionality reduction, and feature extraction is enabled, facilitating more accurate and insightful analysis in the medical domain. There are several types of medical data modalities such as MRI, CT-scan, X-ray, ultra-sound, PET, multi-spectral imaging and retinal imaging. This section reviews the literature on LLRMA applied to the different medical image modalities.

4.1 LLRMA with MRI

Recently, there has been an increasing focus on developing efficient techniques to improve the accuracy of clinical diagnosis by denoising 3D MRI data. Several techniques to denoise 3D MRI data have been suggested in the literature. [123] proposed a novel method that fully exploits the MRI's local and non-local similarity using low-rank tensor approximation. The adaptive low-rank tensor approximation effectively filters the 3D MRI patch stacks, which the adaptive higher-order singular value thresholding (AHOSVT) algorithm solves. While [124] proposed a novel approach for denoising MR images by combining a non-local self-similarity technique with a LRMA method. Another method proposed in [125] is based on LLRMA with regularization of weighted nuclear norm minimization (WNNM) to remove Rician noise from MR images. Since the method proposed in [123] involves tensor matricizations, it lacks flexibility. To overcome this drawback, [126] proposed a method for denoising MR images degraded by Rician noise based on low-rank tensor approximation. [127] performed a similar study as [125]; the authors used weighted Schatten p-norm as a minimization method.

[128] proposed a reconstruction method for multi-contrast imaging and parameter mapping based on a union of local subspace constraint. [129] conducted a study similar to that of [123], incorporating forward and inverse variance stabilizing transforms for the Rician distribution. Both [123] and [129] utilized a denoising technique based on the HOSVD approach. This approach entails calculating transform coefficients using a hard threshold function. This constrains the denoising performance. [130] proposed modified HOSVD

(MHOSVD), which uses a parameterized logarithmic nonconvex penalty function for optimization to overcome this drawback. [131] proposed a denoising method that incorporates an extended difference of Gaussian (DoG) filter and non-local low-rank regularization to denoise an MR image. While [132] proposed a novel structure-constrained LRMA (SLR) method for MRI denoising that exploits geometric information of local MRI image contents and non-local self-similarity of global MRI image structures. The proposed method incorporates two complementary regularization techniques, Kernel Wiener filtering (KWF) and low-rank regularization. On the other hand, [133] proposed a joint denoising method to exploit natural information redundancy in MR diffusion-weighted images (DWIs) through low-rank patch matrix approximation. Finally, [134] proposed a denoising method based on weighted tensor nuclear norm minimization and balanced non-local patch tensors.

4.2 LLRMA with CT-scan

Denoising CT images is a challenging task that requires sophisticated algorithms to reconstruct a noiseless image from a noisy one. [135] proposed a denoising algorithm that uses low-rank sparse coding to reconstruct CT images. This method incorporates non-local self-similarity constraint and group-wise sparse coding noise regularization to reduce sparse coding error. On the other hand, [136] proposed another approach for CT image denoising that takes advantage of the global spatial correlation and local smoothness properties. The suggested approach involves the extraction of overlapping cubic patches, followed by vectorization. Similar patches in the noisy image are then grouped into blocks, forming a third-order tensor. Each corresponding tensor block is subjected to denoising using tensor singular value decomposition (t-SVD), while the preservation of edges and assurance of local smoothness are achieved through the use of total variation (TV). In a related work by [111], a super-resolution model tailored for single 3D medical images was introduced.

Additionally, [137] recently proposed a novel non-local low-rank regularization and data-driven tight-frame CT image reconstruction model (NLLR-DDTF). This model integrates non-local low-rank matrix approximation (NLLRMA) and data-driven tight frame-based regularization for CT image reconstruction. The study combines the advantages of both NLLRMA and data-driven tight frame-based regularization, aiming to improve the accuracy of image reconstruction.

4.3 LLRMA with X-Ray

[110] propose a deformable tracking method based on tensors and model propagation. The proposed method uses tensors and model propagation to solve the multi-dimensional assignment problem. The approach addresses the challenge of tracking anatomical structures and devices prone to appearance change and low visibility in X-ray images. While [138] introduced a denoising technique

for 2D digital subtraction angiography (DSA), employing a weighted local low-rank approach facilitated by an advanced neurovascular replication system. On the other hand, [139] uses photon recycling to denoise ultra-low dose X-ray sequences. The method exploits non-local self-similarity and weighted patch-matching to align similar image regions in current and previous frames. A noise level-based LLRMA and weighted aggregation of the patches are used to produce denoised images. Both methods demonstrate the potential for improving the robustness and accuracy of medical imaging in challenging environments.

4.4 LLRMA with Ultra-sound

[140] proposed two methods of recovering a despeckled 2D image from the speckled data. Despeckling is the process of removing speckle noise while maintaining edge preservation without sacrificing speckle reduction. The LLRMA is the first method used to despeckle ultrasound images (DLRA). This method converts multiplicative noise to additive noise through homomorphic filtering before applying weighted nuclear norm minimization (WNNM) since LLRMA methods for denoising an image are applicable to additive noise. In 2019, [141] proposed an extension of the method. However, the direct extension of this approach disrupts the temporal correlation found in 3D US images, reducing despeckling performance. As a result, the novel method used tensor LLRMA to denoise 3D ultrasound images.

In a similar study, [142] proposed a nonconvex LLRMA model based on non-local similar patch matrices to remove the speckle noise. The proposed method for ultrasound image restoration employs a nonconvex LLRMA model that incorporates the WNNM and data fidelity term.

4.5 LLRMA with PET

In order to apply a tensor LLRMA effectively and efficiently, [143] suggested a non-local tensor low-rank framework for dynamic PET reconstruction using a t-SVD-based technique. The suggested methodology incorporates hidden data and improves optimization efficiency by using an expectation maximization (EM) method as a fidelity term and a TV constraint in addition to the regularization method to extract local structure. Distributed optimization is used to jointly solve a Poisson PET model that combines these regularizations. Beyond spatiotemporal correlation, the Poisson model contains a novel non-local low-rank tensor constraint that captures data correlation in multiple dimensions in dynamic PET. This model recovers highly degraded data and complements structures in low-active frames by leveraging temporal information between frames and non-local self-similarities inside each frame to increase structured sparsity for each image.

In contrast, [144] proposed a PET image denoising method based on LRMA that exploits self-similarity and low-rank of the images. The proposed method pre-filters the original noisy image in the first iteration to improve the selection accuracy of similar patches. However, instead of directly grouping patches

on the pre-filter image in the first iteration, the coordinates of the pre-filter image for the selected patches are recorded. These coordinates are used to group the patches of the noisy image. Then similar patches are grouped as column vectors to form a group matrix estimated using the LRMA method. All denoised patches are aggregated to obtain an initially denoised image. The enhanced back projection technique is applied at each iteration to improve denoising results and retrieve information loss due to a residual image. A final denoised image is obtained after several iterations.

4.6 LLRMA with multispectral imaging

[145] proposed a learning-based approach that takes advantage of multispectral retinal image's spatial and spectral characteristics. The proposed method first represents each pixel's feature vector in each spectral MSI slice using a 2D spatial-spectral matrix. A generalized low-rank matrix approximation (GLRAM) framework is used to solve the feature learning problem. The purpose of GLRAM is to construct low-dimensional, compact representations of a sequence of spatial-spectral matrices. The proposed method creates a 2D spatial-spectral matrix of local binary pattern features to accurately describe the spatial attributes of each spectrum image.

4.7 LLRMA with retinal imaging

[146] proposed a method for drusen segmentation in retinal images, employing a supervised feature learning approach. The technique utilizes GLRAM and supervised manifold regularization to extract discriminative and concise descriptors from image patches extracted from retinal images. The learned features are closely associated with drusen, and potentially may be free of irrelevant information for accurate drusen identification against the background. The support vector machine classifier is used in the final stage of the proposed model to determine the presence of drusen in the pixels of test images.

4.8 LLRMA with a Mixture of modalities

Various methods for enhancing the quality and accuracy of medical images have been suggested in the existing literature. [72] proposed a method that uses LLRMA with NNM constraint and block matching to fuse medical images and overcome distortion and information loss. [73] proposed a kNN-regression method for predicting CT images from MRI data by finding nearest neighbors and using supervised descriptor learning based on LRMA and manifold regularization. In contrast, [147] proposed a method for predicting pseudo-CT images from T1w and T2w MRI data using learned nonlinear local descriptors and feature matching. The method removes bias field artifacts from MR images using a bias correction algorithm. The intensity normalization technique then reduces the variance between MR images from different patients.

Another method proposed in [148] uses non-local self-similar redundancy and low-rank prior techniques to improve the resolution of low-resolution medical images and recover high-resolution images. The proposed method applies low-rank filtering to the group matrices to obtain pixel estimates. A weighted averaging approach is used to handle the issue of multiple estimates for each pixel. They performed a low-rank reconstruction and iteratively applied a sub-sampling consistency constraint to improve the method's performance. These methods enhance medical image analysis and visualization, improving the accuracy of medical diagnosis and treatment.

Table 5 shows a comprehensive summary of similarity measures, low-rank methods, strengths and weaknesses of papers applying LLRMA technique to medical datasets with different modalities.

Table 5 Summary of measure of similarity, low-rank method, source code, strengths, and drawbacks of papers employing LLRMA on medical datasets with different modalities. The term "Not provided" was used for publications where the source code was not provided and we could not find it on the authors' website or github.

References	Year	Application	Measure of Similarity	Low-rank Method	Source code	Strengths	Weakness
Liu et al. [72]	2015	Image fusion	Weighted Euclidean distance	SVD	https://linq.com/4qvCu	<ul style="list-style-type: none"> • Addresses fusion distortion and information loss. 	<ul style="list-style-type: none"> • Applies equal weights to different singular values for low-rank approximation.
Fu et al. [123]	2016	Denoising MRI image	KNN	Tensor approximation	Not provided	<ul style="list-style-type: none"> • Considers non-local spatial self-similarity and cross-slice correlation in 3D MR images 	<ul style="list-style-type: none"> • Lacks flexibility due to tensor matricization [126].
Zhong et al. [73]	2016	Prediction of CT image from MRI	KNN	GLRA	Not provided	<ul style="list-style-type: none"> • Utilizes supervised descriptor learning based on LRMA and manifold regularization to optimize local MR image patch descriptors 	<ul style="list-style-type: none"> • KNN sensitivity to data noise and outliers.
Xia et al. [125]	2017	Denoising MRI images	Block matching	Weighted nuclear norm minimization	Not provided	<ul style="list-style-type: none"> • Employs a flexible thresholding strategy. • Allows image attenuation without losing crucial features. 	<ul style="list-style-type: none"> • Inability to fully exploit correlation among different dimensions in high-dimensional MR data. • Loss of high-frequency components, such as edges and fine structures.
Ren et al. [146]	2017	Binary classification	Distance	GLRA	Not provided	<ul style="list-style-type: none"> • Diminishes image patch dimensionality while enhancing discriminative power. 	<ul style="list-style-type: none"> • Not always practical since it requires a large amount of labelled training data.

Table 5 Cont.

References	Year	Application	Measure of Similarity	Low-rank Method	Source code	Strengths	Weakness
Sagheer et al. [140]	2017	Denoising ultrasound images	Block matching	Weighted nuclear norm minimization	Not provided	<ul style="list-style-type: none"> Includes a preprocessing stage considering statistical properties of ultrasound images. 	<ul style="list-style-type: none"> Extending this method can compromise the temporal correlation in 3D ultrasound images, adversely affecting despeckling performance.
Lei et al. [135]	2018	Denoising CT images	KNN	SVD	Not provided	<ul style="list-style-type: none"> Utilizes group-wise sparse coding for noise minimization. Employs Bayesian interpretation for adaptive parameter learning. 	<ul style="list-style-type: none"> Robustness to different types or levels of noise is not extensively analyzed. Computational requirements are not thoroughly discussed, potentially affecting feasibility.
Hariharan et al. [139]	2018	Denoising X-ray images	Weighted patch matching	SVD	Not provided	<ul style="list-style-type: none"> Enables parallel computing by denoising patches independently. 	<ul style="list-style-type: none"> Denoised images may exhibit mild blurring around instrument edges.
Khaleel et al. [126]	2018	Denoising MRI images	Euclidean distance	t-SVD	Not provided	<ul style="list-style-type: none"> Demonstrates flexibility and computational efficiency compared to traditional techniques. 	<ul style="list-style-type: none"> The proposed method lacks generalizability for different medical image modalities.
Mandava et al. [128]	2018	Reconstruction method for multi-contrast imaging	Subspace basis	SVD	Not provided	<ul style="list-style-type: none"> Utilizes a union of local subspace constraints coupled with a sparsity-promoting penalty. 	<ul style="list-style-type: none"> The reconstruction time for MOCCO-LS is also longer.
Zhai et al. [127]	2018	Denoising MRI images	Block matching	Weighted Schatten p-norm minimization	Not provided	<ul style="list-style-type: none"> The proposed method has a global optimum efficiently solvable by the generalized iterated shrinkage method when weights are in non-decreasing order. 	<ul style="list-style-type: none"> Involves solving a computationally expensive weighted Schatten p-norm minimization problem.

Table 5 Cont.

References	Year	Application	Measure of Similarity	Low-rank Method	Source code	Strengths	Weakness
Yang et al. [147]	2018	Prediction of CT image from MRI	KNN	GLRA	Not provided	<ul style="list-style-type: none"> Utilizes a combination of dense scale-invariant feature transform descriptors and normalized raw patches for MR images, enhancing bone identification capability. 	<ul style="list-style-type: none"> Lacks detailed discussion on the computational requirements, potentially impacting feasibility.
Sagheer et al. [141]	2019	Denoising ultrasound images	l_2 distance	Tensor approximation	Not provided	<ul style="list-style-type: none"> Effectively exploits spatial and temporal correlation in data for denoising. 	<ul style="list-style-type: none"> l_2 distance treats each pixel uniformly, neglecting contextual information and varying intensity significance across regions.
Liu et al. [143]	2019	Denoising CT and MRI images	Euclidean distance	SVD	Not provided	<ul style="list-style-type: none"> Combines low-rank prior and nonlocal self-similar prior with iterative refinement for improved results. 	<ul style="list-style-type: none"> Euclidean distance solely considers pixel intensities, overlooking inherent uncertainty or variability due to noise.
Xie et al. [143]	2019	Denoising and PET reconstruction	Euclidean distance	t-SVD	Not provided	<ul style="list-style-type: none"> Spontaneously exploits inner temporal correlation without tracer information or model fitting. 	<ul style="list-style-type: none"> Limited effectiveness for data with involuntary but noticeable motion. Not guaranteed to perform well in 3D PET reconstruction.
Sagheer et al. [136]	2019	Denoising CT image	l_2 distance	Tensor approximation	Not provided	<ul style="list-style-type: none"> Denoises images using tensor LRMA and tensor total variation technique. 	<ul style="list-style-type: none"> Effectiveness depends on image characteristics, may not be suitable for all types of CT images.

Table 5 Cont.

References	Year	Application	Measure of Similarity	Low-rank Method	Source code	Strengths	Weakness
Hariharan et al. [138]	2019	Denoising X-ray images	Euclidean distance	Weighted low-rank	Not provided	<ul style="list-style-type: none"> • Applies constrained low-rank approximations in both rows and columns. 	<ul style="list-style-type: none"> • The choice of a fixed patch size may not adequately consider anatomic variability.
Lv et al. [129]	2019	Denoising MRI images	KNN	Tensor approximation	Not provided	<ul style="list-style-type: none"> • Exploits non-local and low-rank properties of the grouped image block. 	<ul style="list-style-type: none"> • Denoising methods based on HOSVD constrains the denoising performance [130].
He et al. [145]	2019	Image segmentation	feature point matching	GLRA	Not provided	<ul style="list-style-type: none"> • Enables the learning of patterns closely related to their class labels for generating more discriminative representations. 	<ul style="list-style-type: none"> • The spatial-spectral features of other retinal diseases may vary from those of diabetic retinopathy, potentially affecting the efficacy of the proposed approach.
Yang et al. [144]	2020	Denoising PET images	Euclidean distance	SVD	Not provided	<ul style="list-style-type: none"> • Utilizes an enhanced back-projection step to compensate for the loss of details, improving the denoising result 	<ul style="list-style-type: none"> • As Euclidean distance is not robust to noise in image data, a small amount of noise can significantly impact the distance calculation, resulting in inaccurate similarity measurements.
Wang et al. [130]	2020	Denoising MRI images	Block matching	HOSVD	Not provided	<ul style="list-style-type: none"> • Uses nonconvex logarithmic regularization and nonlocal similarity to apply an adaptive multilinear tensor rank approximation approach. 	<ul style="list-style-type: none"> • The proposed method may not effectively eliminate noise in MR images with very low signal-to-noise ratios.
Zhang et al. [132]	2020	Denoising MRI images	Block matching	SVD	Not provided	<ul style="list-style-type: none"> • Uses a structure-constrained LRMA model that exploits both local and nonlocal priors. 	<ul style="list-style-type: none"> • The method's effectiveness may depend on the specific characteristics of the images to be denoised.

Table 5 Cont.

References	Year	Application	Measure of Similarity	Low-rank Method	Source code	Strengths	Weakness
Yang et al. [142]	2021	Ultrasound image restoration	Euclidean distance	SVD	Not provided	<ul style="list-style-type: none"> • By incorporating the notion of fidelity, the method accounts for the unique characteristics of ultrasound images. 	<ul style="list-style-type: none"> • The choice of a fixed patch size may not sufficiently account for anatomic variability.
Chen et al. [131]	2021	denoising MRI images	Euclidean distance	SVD	Not provided	<ul style="list-style-type: none"> • High-frequency components are retrieved using DoG filter. 	<ul style="list-style-type: none"> • Euclidean distance is based on pixel intensities and does not consider the inherent uncertainty or variability caused by noise.
Chen et al. [124]	2021	Denoising MRI images	Euclidean distance	SVD	Not provided	<ul style="list-style-type: none"> • Produces better approximation especially when the noise level is high. 	<ul style="list-style-type: none"> • The method's sensitivity with respect to parameter settings, i.e., patch size, has not been thoroughly investigated.
Shen et al. [137]	2021	reconstructing CT images	Euclidean distance	SVD	Not provided	<ul style="list-style-type: none"> • Uses an asymmetric treatment for image reconstruction and Radon domain inpainting 	<ul style="list-style-type: none"> • Euclidean distance is based on pixel intensities and does not consider the inherent uncertainty or variability caused by noise.
He et al. [134]	2022	Denoising MRI images	K-means clustering	Tensor approximation	Not provided	<ul style="list-style-type: none"> • Constructs highly correlated 3D non-local patch tensors. • Exploits the effectiveness of t-SVD using balanced 3D non-local patch tensors. 	<ul style="list-style-type: none"> • If the estimate of σ_R is not accurate, the VST conversion may introduce residual errors or distortions that affect denoising performance.
Zhao et al. [133]	2022	Denoising diffusion weighted images	Block matching	SVD	https://github.com/joey024/DWIdenoising	<ul style="list-style-type: none"> • The proposed method has application to other clinical MRI protocols besides diffusion MRI. 	<ul style="list-style-type: none"> • If a large patch window size is used the performance of the method may degrade.
Jia et al. [111]	2022	High-resolution	Euclidean distance	Tensor decomposition	Not provided	<ul style="list-style-type: none"> • Avoids estimation bias caused by the traditional convex procedure. 	<ul style="list-style-type: none"> • Increased computational cost.

5 Medical Datasets Employed with LRMA and LLRMA

Medical image datasets are collections of digital images derived from various imaging technologies such as PET, CT, MRI and others. These datasets serve as valuable resources for training and developing machine-learning algorithms and computer-aided diagnosis systems in the medical domain. In this section, we briefly summarize several medical datasets that have been used for various machine-learning applications.

One such dataset used in various studies [102, 111, 123, 125–127, 129, 130, 134, 148] is the synthetic 3D MRI dataset from the BrainWeb database. This dataset comprises T1-weighted (T1w) data without noise, along with T2-weighted (T2w) data and proton density-weighted (PDw) data associated with the healthy brain. Furthermore, these studies used the real 3D MRI dataset from the open access series of imaging studies (OASIS) data to validate the reliability of the proposed models. There are 416 individuals aged 18 to 96 years, representing a cross-sectional sample. The participants consist of both males and females who are all right-handed. Among the subjects, there are 100 individuals aged sixty and older in the study who have been clinically diagnosed with very mild to moderate Alzheimer's disease (AD).

In addition to the above-mentioned datasets, [126] and [130] used Auckland cardiac MRI Atlas and multi-modal brain tumour image segmentation challenge (BraTS) 2013 databases, respectively. The Auckland cardiac MRI Atlas dataset utilized a 1.5T SIEMENS Avanto MR device to acquire T1-weighted images, true FISP Cines, MR tagging, and contrast MRI. T1-weighted images and true FISP Cines were obtained through a retrospectively controlled steady-state free precession anatomic spin echo sequence, employing a phased array surface coil and ECG R-wave triggering. In contrast, the BraTS database offered pre-optimized MRI datasets through various image preprocessing methods, making them suitable for further applications like CAD segmentations in simulation scenarios. On the other hand, [120] used hyperspectral image data that comprises of 59 data cubes from 59 biopsies, with each biopsy representing a different patient. Among these biopsies, there are 20 normal samples, 19 samples of benign adenoma, and 20 samples of malignant carcinoma colon. Each data cube contains a series of 128 grayscale images captured at a magnification of 400X. The images cover a frequency range of approximately 440 nm to 700 nm. Each image has dimensions of 495 pixels in width and 656 pixels in height.

[149] used a breast cancer dataset that included a total of 208 participants in the breast screening study, categorized as either healthy (asymptomatic) or sick (symptomatic). The sick patients were diagnosed with breast cancer or non-cancerous conditions with symptoms using clinical breast examination (CBE) and mammography. The median age of the participants in the study was 60 years, and they represented different ethnicities: 77 (37%) were Caucasian, 57 (27.4%) were African, 72 (34.6%) were Pardo, 1 (0.5%) was Mulatto, and

1 (0.5%) was indigenous. All participants underwent infrared imaging using a FLIR thermal camera (model SC620). The acquired images had a spatial resolution of 640×480 pixels. While [139] used 20 clinical sequences consisting of 3 different sites, 7 patients, and 500 images. These sequences were acquired with a significantly reduced radiation dose, called ultra-low dose, set at 50% of the standard low dose. These clinical ultra-low-dose sequences were acquired during cardiac and renal electrophysiological procedures (EP). Image sequences were acquired with a matrix size of either 1024×1024 or 960×960 and at a rate of 3 frames per second. [110] used X-ray fluoroscopic sequences from 17 clinical cases, with data acquired at a pixel size of 512×512 and a resolution of $0.4313\text{mm} \times 0.3450\text{mm}$.

[141] used three datasets, including real 3D ultrasound images and two distinct sets of simulated ones. The real 3D ultrasound data comprises images captured pre and post tumor resection, whereas the simulated data comprises phantom images with dimensions of $128 \times 128 \times 128$ and images with a frequency of 20Hz sized at $512 \times 512 \times 3$, respectively. [137] used a head image with smaller details, a head image and a brain image with more details to evaluate the proposed method. [138] used X-ray sequences obtained at three different concentration levels of the contrast agent and four different dose levels of the standard dose level. [146] used a STARE and DRIVE database; the STARE database contained 400 retinal fundus images of the retina, each with a size of 700×605 . Sixty-three images were clinically found to contain drusen, while the DRIVE database contained 40 RGB color retinal images; each image is 768×584 . [71] used the brain atlas database, which contained sections on the normal brain, cerebrovascular disease, neoplastic disease, degenerative disease, and infectious disease of MR and PET images. [145] employed MSI comprising 40 sequences indicative of unhealthy conditions and ten sequences representing healthy conditions. These sequences captured images of the oculus dexter (OD) or oculus sinister (OS) from a cohort of 20 patients diagnosed with diabetic retinopathy (DR) and five healthy subjects. The images were in DICOM format with a bit depth of 16, each having dimensions of 2048×2048 . [124] and [131] used T2 MR data obtained from a healthy volunteer with fast-field-echo sequences: triceps surae of $1050/8.3\text{ms}$, field of view of $280 \times 280\text{mm}^2$, flip angle of 111° . [102] used a single slice of MR fingerprinting data of a healthy volunteer's brain acquired with a 3T Skyra scanner. [98] employed three-dimensional optical coherence tomography (OCT) images centered on the macula, obtained using the Topcon 3D OCT-1000 scanner. Each 3D OCT image consisted of 64 two-dimensional scans, each with dimensions of 480×512 pixels.

Table 10 This table provides an overview of the various datasets. Each dataset is described by a brief data description, the type of data, the tasks that can be performed on the dataset, the tasks performed, the links to access the dataset, and the publications that have used the data. The “x” symbol indicates that the possible tasks have not been performed on that dataset, while “✓” indicates that the task has been performed on that particular dataset. Where dataset information was missing on a particular publication, the term “Not provided” was used for columns such as “Data description”, “Data source” and “Dataset” while the term “Not applicable” was used in the “Task” and “Performed task” columns due to the missing information.

Dataset	Data description	Data type	Task	Performed task	Data source	Publications using this dataset
Synthetic 3D BrainWeb MRI	Comprises T1w and T2w data without noise and a PDw data corresponding to the healthy brain.	Images	<ul style="list-style-type: none"> •Image segmentation •Classification •Image denoising •Multi-modal fusion 	x x ✓ x	http://brainweb.bic.mni.mcgill.ca/brainweb	Fu et al. [123], Xia et al. [125], Zhai et al. [127], Khaleel et al. [126], Asslander et al. [102], Lv et al. [129], Liu et al. [148], Wang et al. [130], Chen et al. [131], He et al. [134]
Real 3D MRI (OASIS)	Includes 416 cross-sectional subjects (aged 18-96) with 3-4 T1-weighted MRI scans per subject, including both right-handed men and women. It also features 100 subjects over 60 diagnosed with very mild to moderate Alzheimer’s disease and a reliability subset of 20 nondemented subjects imaged within 90 days.	Images	<ul style="list-style-type: none"> •Image segmentation •Classification •Image denoising •Multi-modal fusion 	x x ✓ x	http://www.oasis-brains.org/	Fu et al. [123], Xia et al. [125], Zhai et al. [127], Khaleel et al. [126], Lv et al. [129], Wang et al. [130], He et al. [134], Jia et al. [111]
AMRG Cardiac MRI Atlas	The dataset comprises a labeled collection of MRI images depicting the heart of a healthy patient.	Images	<ul style="list-style-type: none"> •Image segmentation •Classification •Image denoising •Multi-modal fusion 	x x ✓ x	https://www.cardiacatlas.org/amrg-cardiac-atlas/	Khaleel et al. [126]
BraTS	Not provided	Images	Not applicable	Not applicable	Not provided	Wang et al. [130]
Not provided	Not provided	Images	Not applicable	Not applicable	Not provided	Chen et al. [131]
Real 3D CT	Not provided	Images	<ul style="list-style-type: none"> •Image segmentation •Classification •Image denoising •Multi-modal fusion 	x x ✓ x	http://www.via.cornell.edu/databases	Sagheer et al. [136]

Table 10 Cont.

Dataset	Data description	Data type	Task	Performed task	Data source	Publications using this dataset
Low dose CT	Not provided	images	<ul style="list-style-type: none"> •Image segmentation •Classification •Image denoising •Multi-modal fusion 	x x ✓ x	http://www.aapm.org/GrandChallenge/LowDoseCT/	Sagheer et al. [136]
Simulated brain DWI	Not provided	Images	Not applicable	Not applicable	Not provided	Zhao et al. [133]
In vivo human brain DWI	Not provided	Images	Not applicable	Not applicable	Not provided	Zhao et al. [133]
T2 MR data	Obtained from a healthy volunteer with fast-field-echo sequences: triceps surae of 1050/8.3ms, field of view of 280 × 280mm ² , flip angle of 111°.	Images	<ul style="list-style-type: none"> •Image segmentation •Classification •Image denoising •Multi-modal fusion 	x x ✓ x	Not provided	Chen et al. [124], Chen et al. [131]
DSC-MRI brain perfusion sequence	Not provided	Images	Not applicable	Not applicable	Not provided	Ulas et al. [104]
in-vivo breath-hold cardiac perfusion sequence	Not provided	Images	Not applicable	Not applicable	Not provided	Ulas et al. [104]
Cardiac perfusion	Not provided	Images	Not applicable	Not applicable	https://ca2r.net/resources/	Xu et al. [105]
Cardiac cine	Not provided	Images	Not applicable	Not applicable	https://ca2r.net/resources/	Xu et al. [105]
In-vivo MRI data	Not provided	Images	Not applicable	Not applicable	http://shorty.usc.edu/class/591/fall04/	Lyra et al. [94]
Multicontrast multichannel 2D human brain datasets	Not provided	Images	Not applicable	Not applicable	Not provided	Yi et al. [109]
CT images	Not provided	Images	Not applicable	Not applicable	Not provided	Lei et al. [135]
CT images	A head image with smaller details, a head image and a brain image with more details.	Images	Not applicable	Not applicable	Not provided	Shen et al. [137]

Table 10 Cont.

Dataset	Data description	Data type	Task	Performed task	Data source	Publications using this dataset
	The image sequences were acquired at 3 frames per second. There were 20 clinical sequences, that is, 7 patients and 500 clinical images.	Images/video	<ul style="list-style-type: none"> •Image segmentation •Classification •Image denoising •Object detection 	x x ✓ x	Not provided	Hariharan et al. [139]
X-ray images	X-ray fluoroscopic sequences obtained from 17 clinical cases.	Images/video	<ul style="list-style-type: none"> •Image segmentation •Classification •Image denoising •Tracking of deformable objects 	x x x ✓	Not provided	Cheng et al. [110]
X-ray images	X-ray sequences are obtained at three different concentration levels of the contrast agent and four different dose levels of the standard dose level.	Images/video	<ul style="list-style-type: none"> •Image segmentation •Classification •Image denoising •Dose optimization 	x ✓ x x	Not provided	Hariharan et al. [138]
	A single slice MR fingerprinting data of a healthy volunteer's brain that was acquired with a 3T Skyra scanner.	Images	<ul style="list-style-type: none"> •Image segmentation •Classification •Image denoising •Image reconstruction 	x x x ✓	Not provided	Asslander et al. [102]
Real ultrasound data	Not provided	Images/video	Not applicable	Not applicable	Not provided	Sagheer et al. [140]
Simulated ultrasound data	Not provided	Images/video	Not applicable	Not applicable	Not provided	Sagheer et al. [140]
Simulated ultrasound images	Not provided	Images	Not applicable	Not applicable	Not provided	Yang et al. [142]
Real ultrasound images	Not provided	Images	Not applicable	Not applicable	Not provided	Yang et al. [142]
Digital mouse phantom	Not provided	Images	Not applicable	Not applicable	Not provided	Yang et al. [144]
Human brain phantom	Not provided	Images	Not applicable	Not applicable	Not provided	Yang et al. [144]

Table 10 Cont.

Dataset	Data description	Data type	Task	Performed task	Data source	Publications using this dataset
Real 3D ultrasound data	Consist of three dimensional ultrasound images before and after tumor resection.	Images	<ul style="list-style-type: none"> •Image segmentation •Classification •Image denoising •Image reconstruction 	x x ✓ x	http://www.bic.mni.mcgill.ca/	Sagheer et al. [141]
Simulated 3D ultrasound data	consist of phantom images corresponding to a size of $128 \times 128 \times 128$.	Images	<ul style="list-style-type: none"> •Image segmentation •Classification •Image denoising •Image reconstruction 	x x ✓ x	https://in.mathworks.com/matlabcentral/	Sagheer et al. [141]
Simulated 3D ultrasound data	consist of simulated 3D images at a frequency of 20Hz of size $512 \times 512 \times 3$.	Images	<ul style="list-style-type: none"> •Image segmentation •Classification •Image denoising •Image reconstruction 	x x ✓ x	http://splab.cz/en/research/zpracovani-medicinskyh-signalu/databaze/artery	Sagheer et al. [141]
Zubal head phantoms	Not provided	Images	Not applicable	Not applicable	Not provided	Xie et al. [143]
Real Cardiac data	Not provided	Images	Not applicable	Not applicable	Not provided	Xie et al. [143]
CT lung data	Not provided	Images	Not applicable	Not applicable	Not provided	Liu et al. [148]
CT cardiac data	Not provided	Images	Not applicable	Not applicable	Not provided	Liu et al. [148]
T1, T2 weighted MRI	Not provided	Images	Not applicable	Not applicable	Not provided	Zhong et al. [73], Yang et al. [147], Peng et al. [103]
CT images	Not provided	Images	Not applicable	Not applicable	Not provided	Zhong et al. [73], Yang et al. [147]
MSI images	Consist of 40 sequences indicative of unhealthy conditions and ten sequences representing healthy conditions. The images were in DICOM format with a bit depth of 16, each having dimensions of 2048×2048 .	Images	<ul style="list-style-type: none"> •DR lesion segmentation •Classification •Image denoising •Image reconstruction 	✓ x x x	Not provided	He et al. [145]

Table 10 Cont.

Dataset	Data description	Data type	Task	Performed task	Data source	Publications using this dataset
STARE database	It contains 400 retinal fundus images of the retina, each image having a size of 700×605 . Sixty-three images were clinically found to contain drusen.	Images	<ul style="list-style-type: none"> •Image segmentation •Classification • Optic disc localization •Generic lesion detection 	x ✓ x x	http://cecas.clemson.edu/~ahoover/stare/	Ren et al. [146]
DRIVE database	It contains 40 RGB color retinal images; each image is 768×584 .	Images	<ul style="list-style-type: none"> •Image segmentation •Classification • Optic disc localization •Generic lesion detection 	x ✓ x x	https://www.isi.uu.nl/Research/Databases/	Ren et al. [146]
Hyperspectral image	Comprises 59 sets of data cubes obtained from 59 biopsies, with each biopsy representing a different patient. Among these biopsies, there are 20 normal samples, 19 samples of benign adenoma, and 20 samples of malignant carcinoma colon.	Images	<ul style="list-style-type: none"> •Target detection •Classification • Anomaly detection •Image compression 	x ✓ x ✓	Not provided	Mahoney et al. [120]
Brain atlas	Contains the sections on normal brain, cerebrovascular disease, neoplastic disease, degenerative disease, and infectious disease of MR and PET images	Images	<ul style="list-style-type: none"> •Image segmentation •Classification •Image denoising •Multi-modal fusion 	x x x ✓	http://www.med.harvard.edu/AANLIB/home.html	He et al. [71]
Infrared images	A total of 208 individuals were included in the study for breast screening, consisting of both healthy individuals without symptoms and individuals with symptoms.	Images	<ul style="list-style-type: none"> •Image segmentation •Classification •Image denoising •Lesion Detection 	x ✓ x x	Not provided	Yousefi et al. [149]
Real clinical data	Not provided	Images	Not applicable	Not applicable	Not provided	Ji et al. [150]
OCT	OCT images of normal eyes acquired with the Topcon 3D OCT-1000 scanner	Images	<ul style="list-style-type: none"> •Image segmentation •Image compression •Image despeckling •Classification 	x ✓ ✓ x	https://pan.baidu.com/share/init?surl=edkG7k8W3Wkjhq8vffCYng	Kopriva et al. [98]

6 Similarity Measure Algorithms

We delve into various similarity measures that can be utilized for medical data analysis and pattern recognition in general. The concept of similarity measures play a crucial role in various fields of study, such as data mining, ML, and information retrieval. Similarity measures are used to quantify the degree of relatedness between two data points based on some specified criteria. In medical data analysis, data embeddings can be used to represent relationships between medical conditions and symptoms. For instance, an embedding could be created to show that the symptom of chest pain is related to the medical condition of myocardial infarction, while shortness of breath is related to heart failure. This is in line with the medical notion of disease categorization and conceptual hierarchies, which can aid in diagnosis, treatment planning, and patient outcomes. By using latent representations in medical data analysis, healthcare professionals can identify patterns, cluster similar conditions together, and make informed decisions. Thus, deriving similarities whether among physical concepts or abstract ones is very important in pattern recognition. Similarity measures are also used in LLRMA to find similar patches in a medical image when a LRMA is in effect for denoising, dimension reduction or compression, feature extraction and etc.

This section discusses in detail five different similarity measure algorithms that are used in the LLRMA methods applied to medical data discussed in Section 4. These similarity measures include the K-nearest neighbor (KNN) algorithm [151], K-means clustering [152], Euclidean distance [153] and weighted Euclidean distance [154], weighted patch matching [155], and block matching using l_1 norm or Manhattan distance [156]. We will provide an in-depth explanation of each method, its advantages and limitations, and its specific use cases. By understanding the characteristics and performance of these similarity measures, we hope researchers and practitioners can choose the most appropriate measure while using LLRMA.

6.1 Distance Measures

In pattern recognition and ML, a distance measure as stated in Eq. 1, quantifies the degree of relatedness between two objects on their features or attributes [157–159]. Distance measures are often referred to as distance functions or metrics. They are used to compare the degree of similarity or difference between two data points, and they are a fundamental component of many learning algorithms. A distance function assigns a numerical value to the similarity between two objects (we are using it in the broadest sense to refer to things that can be represented in a mathematically measurable space), with a smaller value indicating a higher degree of similarity and a larger value indicating a higher degree of dissimilarity. We have shown a geometric illustration of this notion in Fig. 2 and Fig.3.

$$d : X \times Y \rightarrow \mathbb{R}_{\geq 0}. \quad (1)$$

There are various types of distance measures (in fact there is a whole field called Measure Theory dedicated to this and more such as volume, probability, and Lebesgue measure), including the Euclidean distance, Manhattan distance, and Hamming distance [160–163]. Each distance measure has its own mathematical formulation, and is appropriate for different types of data, depending on the specific features or attributes being compared [159]. The choice of a suitable distance measure is essential in ensuring the accuracy and effectiveness of learning algorithms in various applications. In order for a function to be considered a valid distance measure, it must satisfy four key properties:

- Non-negativity: If $d(\mathbf{a}, \mathbf{b})$ is the distance between points $\mathbf{a} \in X$ and $\mathbf{b} \in Y$, then $d(\mathbf{a}, \mathbf{b}) \geq 0$.
- Identity: If $\mathbf{a} \in X$ and $\mathbf{b} \in Y$ are identical points, then $d(\mathbf{a}, \mathbf{b}) = 0$.
- Symmetry: If $\mathbf{a} \in X$ and $\mathbf{b} \in Y$ are any two points, then $d(\mathbf{a}, \mathbf{b}) = d(\mathbf{b}, \mathbf{a})$.
- Triangle inequality: If $\mathbf{a} \in X$, $\mathbf{b} \in Y$, and $\mathbf{c} \in Z$ are any three points, then $d(\mathbf{a}, \mathbf{b}) + d(\mathbf{b}, \mathbf{c}) \geq d(\mathbf{a}, \mathbf{c})$.

These four properties ensure that a *true* distance measures a valid mathematical function and produces meaningful and consistent results. Distance measures satisfying these properties are commonly used in various applications, such as clustering, classification, and pattern recognition.

The Euclidean distance (often referred to as the l_2 norm) and cosine similarity are two commonly used measures of similarity between vectors in tensor analysis [153]. Euclidean distance is a measure of the straight-line distance between two points in an n -dimensional space, while cosine similarity measures the cosine of the angle between two vectors. The relationship between these two measures can be understood through their mathematical connection, which arises from the geometric interpretation of vectors. In particular, given two vectors \mathbf{a} and \mathbf{b} , the Euclidean distance $d_E(\mathbf{a}, \mathbf{b})$ between them is given by the square root of the sum of the squared differences in their coordinates, i.e.,

$$d_E(\mathbf{a}, \mathbf{b}) = \sqrt{\sum_{i=1}^n (\mathbf{a}_i - \mathbf{b}_i)^2} \quad (2)$$

$$= \sqrt{(\mathbf{a} - \mathbf{b}) \cdot (\mathbf{a} - \mathbf{b})}. \quad (3)$$

On the other hand, cosine similarity is given by the dot product of the two vectors, normalized by the product of their magnitudes, i.e.,

$$\cos(\theta) = \frac{\mathbf{a} \cdot \mathbf{b}}{\|\mathbf{a}\| \|\mathbf{b}\|}. \quad (4)$$

The cosine similarity can be related to the Euclidean distance by the identity

$$\cos(\theta) = \frac{\mathbf{a} \cdot \mathbf{b}}{\|\mathbf{a}\| \|\mathbf{b}\|} \quad (5)$$

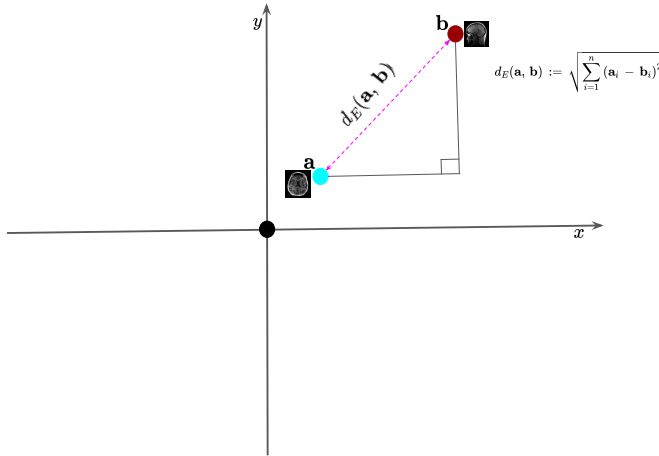


Fig. 2 The Euclidean distance is a commonly used measure of similarity between two points in a Euclidean space. It is defined as the square root of the sum of the squared differences between the corresponding coordinates of the two points as shown in this illustration where \mathbf{a} and \mathbf{b} are two vectors in \mathbb{R}^2 . These can be, for example, representations of two MRI scans as depicted in this figure. However, this notion generalizes to \mathbb{R}^n .

$$= \frac{\sum_{i=1}^n a_i b_i}{\sqrt{\sum_{i=1}^n a_i^2} \sqrt{\sum_{i=1}^n b_i^2}}, \quad (6)$$

which shows that the cosine similarity is a normalized version of the dot product of the vectors. Therefore, while Euclidean distance measures the absolute distance between two vectors, cosine similarity measures their relative orientation. These measures are often used in combination with ML algorithms such as k-means clustering, nearest neighbor classification, and LLRMA where they play complementary roles in measuring similarity and distance.

6.2 Euclidean Distance and Weighted Euclidean Distance

The Euclidean distance can be used to measure the similarity between two vectors with respect to their magnitude and direction. However, the weighted Euclidean distance (WED) is a modification of Euclidean distance, where each coordinate of the vectors is multiplied by a weight factor. These weights are used to adjust the contribution of each coordinate to the distance measure. This is computed as:

$$d_w(\mathbf{a}, \mathbf{b}) = \sqrt{\sum_{i=1}^n \mathbf{w}_i (\mathbf{a}_i - \mathbf{b}_i)^2}, \quad (7)$$

where \mathbf{a} and \mathbf{b} are two vectors of dimension n and \mathbf{w}_i is the weight factor associated with the i th coordinate.

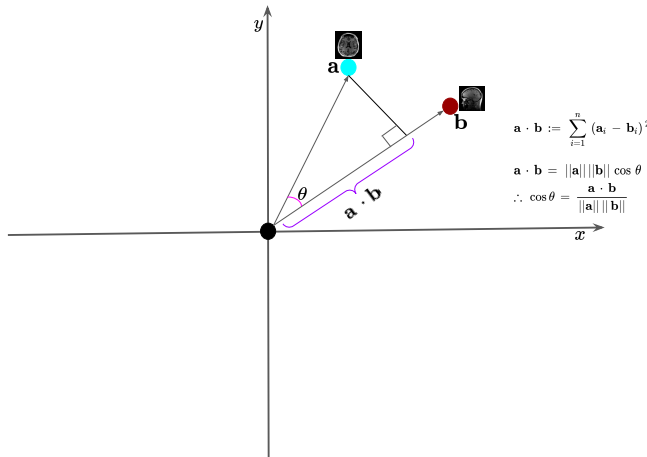


Fig. 3 The dot product between two vectors (\mathbf{a} and \mathbf{b}), is defined as the sum of the products of their corresponding components. As shown in the figure, it is related to the Euclidean distance.

The WED is commonly used in fields such as data mining and image processing, where the data may have a non-uniform distribution or varying importance of the features. The weights can be used to emphasize the importance of certain features or to reduce the impact of irrelevant or noisy features. Both Euclidean distance and WED are useful measures of similarity between vectors and can be applied to a variety of fields, including ML, pattern recognition, and data analysis.

6.3 K-Nearest Neighbors

K-Nearest Neighbors (K-NN) is a widely used ML algorithm in data analysis for classification and regression problems [164–167]. The K-NN algorithm is a non-parametric and lazy (instance-based) learning method that does not make any assumptions about the underlying data distribution. The basic idea behind K-NN is to find the K-nearest neighbors to a given data point (which we shall call a *query*) based on a distance metric and use the labels of those neighbors to classify or predict the label of the given data point as shown in Algorithm 1. In the case of classification, the majority vote of the K-nearest neighbors is taken as the predicted label of the data point, while in regression, the average of the K-nearest neighbors' labels is taken as the predicted value.

To apply the K-NN algorithm, we first need to choose an appropriate distance metric. In medical data analysis, the Euclidean distance and WED are commonly used as distance metrics.

However, in some cases, not all features in the data may be equally important. For instance, in medical data analysis, some features may be more clinically relevant than others. In such cases, K-NN uses a WED, which assigns

Algorithm 1 K-Nearest Neighbors

Require: Dataset $X = \{(\mathbf{x}_1, y_1), (\mathbf{x}_2, y_2), \dots, (\mathbf{x}_n, y_n)\}$, query point \mathbf{x} , number of neighbors K , distance metric $d(x, y)$

- 1: Initialize distances array $D = []$
- 2: **for** $i = 1$ **to** n **do**
- 3: Compute distance $d_i = d(\mathbf{x}, \mathbf{x}_i)$
- 4: Append distance $D.append(d_i)$
- 5: **end for**
- 6: Sort D in ascending order
- 7: Get the first K distances in D : D_K
- 8: Get the indices of D_K : I_K
- 9: **if** classification **then**
- 10: $y = \text{mode}(y_i \mid i \in I_K)$
- 11: **else if** regression **then**
- 12: $y = \text{mean}(y_i \mid i \in I_K)$
- 13: **end if**
- return** Predicted label y

different weights to each feature based on its importance. The weights can be assigned based on domain knowledge or learned from the data using techniques such as principal component analysis (PCA). We have shown a visual illustration of the K-NN algorithm in Fig. 4. In the K-NN algorithm, the choice of K is a hyperparameter that needs to be tuned since it can lead to overfitting or underfitting depending on the value. Methods such as cross-validation or grid search can be used to obtain the optimal value of K . The choice of distance metric, such as Euclidean distance and WED, and the value of K need to be carefully chosen based on the specific problem and data at hand.

6.4 K-Means Clustering

K-means clustering is a commonly used technique in various domains, including medical data analysis [168–170]. The goal of K -means clustering is to group similar data points together based on their features. As shown in Algorithm 2, an initial guess of K centroids of the clusters is given and then each point is iteratively assigned to its nearest centroid based on a distance metric such as Euclidean distance, and the centroid is updated based on the mean of the assigned data points within a given cluster.

The algorithm iterates until convergence, typically determined by a stopping criterion such as a maximum number of iterations or when the change in the centroids falls below a certain threshold. We have illustrated this approach to clustering a 1D feature space in Fig. 5. K-means clustering is a computationally efficient algorithm and can handle large datasets. However, its performance can be sensitive to the initial choice of centroids and the number of clusters. Additionally, k-means clustering assumes that clusters are spherical and equally sized, which may not always be true in practice.

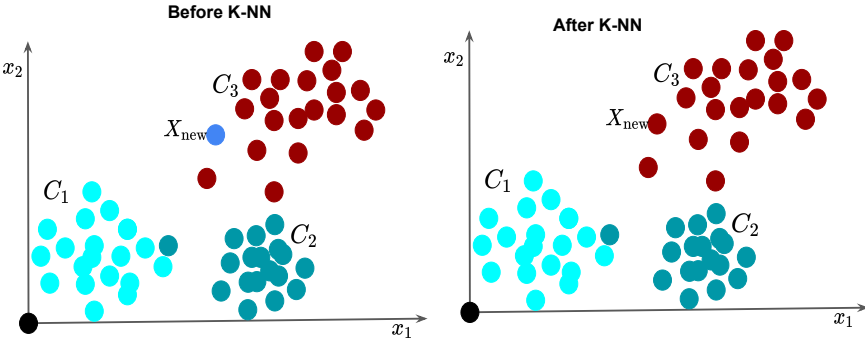


Fig. 4 (Left) A 2D feature visualization of a dataset that comprises three classes (C_1, C_2, C_3). The colors indicate the class labels. With a new datapoint X_{new} , the objective of the K-NN algorithm is to find the class C_i to which the datapoint can be classified based on its K neighbors labels. (Right) After computing the distance between the query X_{new} and all the samples in the dataset, it has been classified into class C_3 which comprises a majority of the new sample neighbors.

Algorithm 2 K-Means Clustering

Require: Number of clusters K , dataset $(\mathbf{x}_1, \mathbf{x}_2, \dots, \mathbf{x}_n)$

```

1: Initialize centroids  $\boldsymbol{\mu}_1, \boldsymbol{\mu}_2, \dots, \boldsymbol{\mu}_K$ 
2: repeat
3:   for  $i = 1$  to  $n$  do
4:     Compute distances:  $d_j = \|\mathbf{x}_i - \boldsymbol{\mu}_j\|^2$ 
5:     Assign sample:  $c_i = \arg \min_j d_j$ 
6:   end for
7:   for  $j = 1$  to  $K$  do
8:     Update centroid:
9:      $\boldsymbol{\mu}_j = \frac{1}{n_j} \sum_{i=1}^n \mathbf{x}_i \cdot \delta c_i, j$ 
9:   end for
10:  until convergence

```

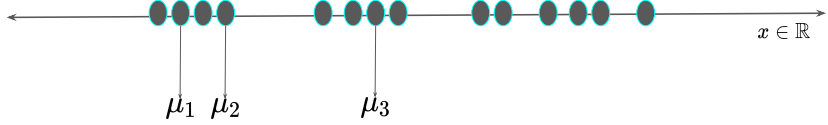
6.5 Weighted Patch Matching

Weighted Patch Matching (WPM) is an effective technique for measuring similarity which can be applied to medical image analysis [171, 172]. It is based on matching small image patches between a reference image I_R and a target image I_T using weighted feature vectors [173]. To do this, we first extract corresponding patches P_i^R and P_j^T from the reference and target images respectively. Each patch is represented by a feature vector f_i^R and f_j^T containing intensity,

Given a dataset:

$$\mathcal{D} = \{x_i \in \mathbb{R} \mid i = 1, 2, \dots, n\}$$

Step 1: Choose $K = 3$ $\mu \sim \mathcal{U}(\mathcal{D}, K)$



Step 2: repeat until convergence

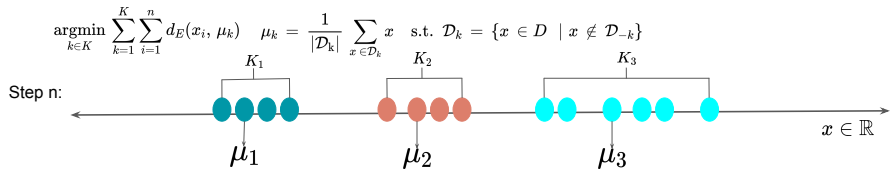
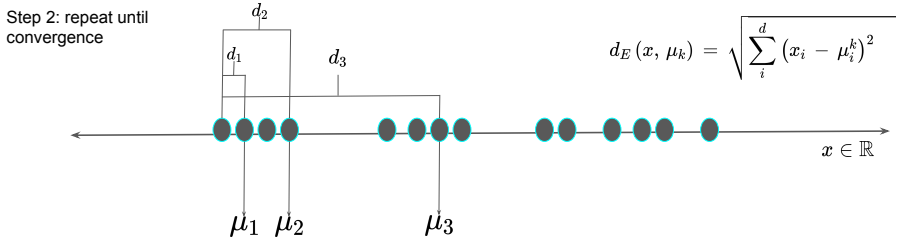


Fig. 5 A visual illustration of K -Means clustering on a 1D dataset where we have $n = 14$ samples and the cluster centroids, $K = 3$. In this formulation, the initial centroids are uniformly randomly chosen as indicated by the vector means $\mu \sim \mathcal{U}(\mathcal{D}, K)$ as indicated in step 1. The distance $d_E(x_i, \mu_i)$ is computed and the sample x_i is assigned to the cluster with the minimum distance as shown in the figure where sample x_1 is assigned to cluster 1. The new cluster centroids are computed from the updated cluster assignment such that the mean μ_k of cluster k is all samples that belong to that cluster. This step is repeated until convergence. Finally, all samples have been properly clustered as indicated by step n in the figure where the colors indicate the clusters to which each data point belongs.

gradient, or other information. To provide robustness against intensity variations, a weight vector w_i^R is computed for each reference patch based on the gradient magnitude:

$$w_i^R(k) = \frac{\nabla I_R(i+k)_2}{\max_k \nabla I_R(i+k)_2},$$

where k indexes the pixels in the patch P_i^R . The weighted feature vector is:

$$\hat{f}_i^R = w_i^R \odot f_i^R.$$

The distance between two patches is then computed as:

$$d(P_i^R, P_j^T) = \hat{f}_i^R - f_j^T \cdot 2.$$

By minimizing d , we find corresponding patches that match well in terms of weighted features, even if the raw intensity values differ. We have shown the conceptual steps for WPM in Algorithm 3.

WPM is well-suited for medical image analysis tasks like registration and segmentation. It can match patches despite differences in scanner modalities or image intensities. The gradient-based weights emphasize edges and textures while suppressing flat regions. This focuses the matching on perceptually relevant structures. For example, WPM has been applied to align magnetic resonance (MR) and transrectal ultrasound (TRUS) images for targeted prostate biopsy. It outperformed standard patch matching due to its ability to handle intensity variations between modalities [174]. WPM has also been used to improve atlas-based segmentation of abdomen CT scans, providing accuracy comparable to interactive segmentation [175].

Algorithm 3 Weighted Patch Matching (WPM)

```

Extract patches  $P_i^R$  from reference image  $I_R$  and  $P_j^T$  from target image  $I_T$ 
for  $i = 1$  to  $N_R$  do
    Compute feature vector  $f_i^R$  for patch  $P_i^R$ 
    Compute weight vector  $w_i^R$  based on  $\nabla P_i^R$ 
    Compute weighted feature  $\hat{f}_i^R = w_i^R \odot f_i^R$ 
    for  $j = 1$  to  $N_T$  do
        Compute distance  $d(P_i^R, P_j^T)$  between  $\hat{f}_i^R$  and  $f_j^T$ 
    end for
    Find  $k = \arg \min_j d(P_i^R, P_j^T)$ 
    Match  $P_i^R$  to  $P_k^T$ 
end for

```

Overall, WPM is a versatile technique for medical image-matching problems where robustness to intensity variations is critical. Its continued development, including learning-based weight optimization and integration with deep networks, will likely extend its applicability even further.

6.6 Block Matching

Block Matching is a widely used technique for estimating correspondences between images by matching small local blocks or patches. In medical imaging, it can be highly effective for tasks like inter-frame motion tracking and deformable image registration. One particularly useful variant utilizes the l_1 norm as the block similarity metric to provide robustness against outliers [176].

The key idea in Block Matching is to divide the reference image I_R and target image I_T into smaller blocks B_i^R and B_j^T of pixels respectively, as shown in Algorithm 4 lines 1-2. The goal is then to find correspondences between individual blocks from I_R and semantically similar blocks in I_T . To enable numeric comparison, each image block is represented by a feature vector f_i^R

and f_j^T capturing intensities, gradients, textures, or other descriptive features (see lines 4-9, Algorithm 4).

A distance metric between feature vectors is then used to quantify block similarity. Using the l_1 norm, $\|\cdot\|_1$ defined as:

$$d(B_i^R, B_j^T) = \|f_i^R - f_j^T\|_1 \quad (8)$$

$$= \sum_{k=1}^n |f_i^R(k) - f_j^T(k)|, \quad (9)$$

provides a robust block comparison that is less influenced by outlier feature differences compared to the l_2 norm [176]. Here, n denotes the dimensionality of the block feature vectors. By minimizing the l_1 distance (lines 12-19), the best matching target block B_j^T can be found for each reference block B_i^R [177].

Applying Block Matching with l_1 similarity to medical images is advantageous as intensity values can vary considerably across modalities and between scans due to noise, artifacts, and pathologies. The l_1 metric provides a degree of invariance to such complex conditions.

In summary, Block Matching using l_1 block feature distance is a versatile and robust technique for medical motion estimation and correspondence problems [176, 177]. Key advantages including simplicity, flexibility across modalities, and strong performance under challenging imaging conditions make it well-suited for a variety of clinical applications.

Algorithm 4 Block Matching with l_1 norm

```

1: Divide reference image  $I_R$  into blocks  $B_i^R$ 
2: Divide target image  $I_T$  into blocks  $B_j^T$ 
3: for  $i = 1$  to  $N_R$  do
4:   Compute feature vector  $f_i^R$  for block  $B_i^R$ 
5: end for
6: for  $j = 1$  to  $N_T$  do
7:   Compute feature vector  $f_j^T$  for block  $B_j^T$ 
8: end for
9: for  $i = 1$  to  $N_R$  do
10:   Initialize best match distance  $d_{\min} = \infty$ 
11:   for  $j = 1$  to  $N_T$  do
12:     Compute  $l_1$  distance  $d(B_i^R, B_j^T) = f_i^R - f_j^T 1$ 
13:     if  $d(B_i^R, B_j^T) < d_{\min}$  then
14:        $d_{\min} = d(B_i^R, B_j^T)$ 
15:        $match(B_i^R) = B_j^T$ 
16:     end if
17:   end for
18: end for

```

7 low-rank method

This section delves into the mathematics and applications of the low-rank techniques within the studies reviewed in Sections 3 and 4. The reviewed papers used several types of low-rank techniques such as SVD, weighted SVD, randomized SVD, tensor SVD, and PCA across various medical image data modalities to facilitate tasks such as feature extraction, compression, denoising, decomposition, and more. The low-rank method provides a solid framework for analyzing and processing high-dimensional data by extracting the most relevant information while reducing computational complexity and/or noise.

7.1 Traditional SVD

When an image can be approximated sufficiently well by a low-rank matrix, SVD can be used to find this approximation. This LRMA can be represented more compactly than the original image. SVD decomposes a complex data matrix $\mathbf{A} \in \mathbb{C}^{m \times n}$ into three independent matrices [178–180]:

$$\mathbf{A} = \mathbf{U}\Sigma\mathbf{V}^\dagger \quad (10)$$

$$= \begin{bmatrix} \hat{\mathbf{U}} & \hat{\mathbf{U}}^\delta \end{bmatrix} \begin{bmatrix} \hat{\Sigma} & \mathbf{0} \\ \mathbf{0} & \mathbf{0} \end{bmatrix} \mathbf{V}^\dagger, \quad (11)$$

where $\mathbf{U} \in \mathbb{C}^{m \times m}$ and $\mathbf{V} \in \mathbb{C}^{n \times n}$ are unitary matrices, $\Sigma = \text{diag}(\xi_1, \xi_2, \dots, \xi_m) \in \mathbb{C}^{m \times n}$ is a diagonal matrix of rank m and \dagger denotes a conjugate transpose. The singular values of the matrix \mathbf{A} , which are denoted as ξ_i and lie on the diagonal entries of the matrix Σ , are uniquely determined by \mathbf{A} . These singular values are arranged in a descending order, that is $\xi_1 \geq \xi_2 \geq \xi_3 \dots \geq \xi_m \geq 0$. It is easy to show that $\lambda_i = \sqrt{\xi_i}$ where λ_i denotes the eigenvalues of $\mathbf{A}\mathbf{A}^\dagger$ or $\mathbf{A}^\dagger\mathbf{A}$. The columns of \mathbf{U} and the columns of \mathbf{V} are the left and right singular vectors of \mathbf{A} , respectively. The vectors $\mathbf{u}_i \in \mathbb{C}^m$ and $\mathbf{v}_i \in \mathbb{C}^n$ are the orthonormal eigenvectors of $\mathbf{A}\mathbf{A}^\dagger$ and $\mathbf{A}^\dagger\mathbf{A}$ respectively. Therefore, Eq. 10 can be written as follows

$$\mathbf{A} = \sum_{i=1}^m \xi_i \mathbf{u}_i \mathbf{v}_i^\dagger. \quad (12)$$

If there exists a matrix of rank r such that $0 \leq r \leq m$, then the optimal approximation of \mathbf{A} that preserves the most important features is given by

$$\mathbf{A}_r = \sum_{i=1}^r \xi_i \mathbf{u}_i \mathbf{v}_i^\dagger. \quad (13)$$

When $r = m$ then $\mathbf{A} = \mathbf{A}_r$. Each value of ξ_i quantifies how much the corresponding component $\xi_i \mathbf{u}_i \mathbf{v}_i^\dagger$ contributes in the reconstruction of \mathbf{A} , that is, the larger the value of ξ_i the more $\xi_i \mathbf{u}_i \mathbf{v}_i^\dagger$ contributes to the reconstruction of

A. The SVD technique constructs aLRMA matrix \mathbf{A}_r by solving the following optimization problem:

$$\operatorname{argmin}_{\mathbf{A}_r, \text{ s.t. } \text{rank}(\mathbf{A}_r)=r} \|\mathbf{A} - \mathbf{A}_r\|_F = \mathbf{U}_r \mathbf{\Sigma}_r \mathbf{V}_r^\dagger, \quad (14)$$

where $\mathbf{U}_r, \mathbf{V}_r$ denotes the first r leading columns of \mathbf{U} and \mathbf{V} , $\mathbf{\Sigma}_r$ denotes a sub-matrix of $\mathbf{\Sigma}$ and $\|\cdot\|_F$ denotes the Frobenius norm. Fig. 6 demonstrates the steps in full and truncated SVD.

The main strength of SVD is its ability to reduce the dimensionality of data, which is particularly useful for tasks involving large datasets. By approximating complex matrices with simpler matrices, SVD enables efficient feature extractions, compression and noise reduction, improving signal quality and/or image processing techniques. However, SVD has its drawbacks. The computational cost of full SVD is relatively high in terms of time and memory. Its time complexity is typically $\mathcal{O}(mn \min\{m, n\})$ [79–84]. In terms of memory, it requires $\mathcal{O}(mn)$ to store the three component matrices [82–85]. The full SVD provides a complete representation of the original matrix and preserves all information that may be important for certain applications. However, it can be impractical for large datasets due to the high computational requirements. The truncated SVD, on the other hand, approximates the original matrix by retaining only r singular values and their corresponding columns from \mathbf{U}_r and \mathbf{V}_r^\dagger . This significantly reduces the computational cost. The time complexity of truncated SVD is approximate $\mathcal{O}(mnr)$ [81–85], and its memory complexity is $\mathcal{O}(r(m + n))$ [82, 83, 85, 181]. The truncated SVD is well suited for dimensionality reduction and noise reduction tasks, where the lower-dimensional approximation captures the most important features of the data. However, some information is discarded in the process, which can lead to a loss of accuracy in certain applications. In addition, the assumption of orthogonal data in SVD may not be true for all datasets, limiting its effectiveness in capturing the underlying structures.

7.2 Weighted SVD

Weighted SVD is a method for matrix factorization that extends the standard SVD method [182]. The weighted matrix, $\tilde{\mathbf{A}}$ with respect to the diagonal weight matrix \mathbf{W} is defined as

$$\tilde{\mathbf{A}} = \mathbf{W} \odot \mathbf{A}, \quad (15)$$

where \odot denotes the Schur product [183]. The weighted SVD of $\tilde{\mathbf{A}}$ is expressed as

$$\tilde{\mathbf{A}} = \mathbf{U} \mathbf{\Sigma}^w \mathbf{V}^\dagger, \quad (16)$$

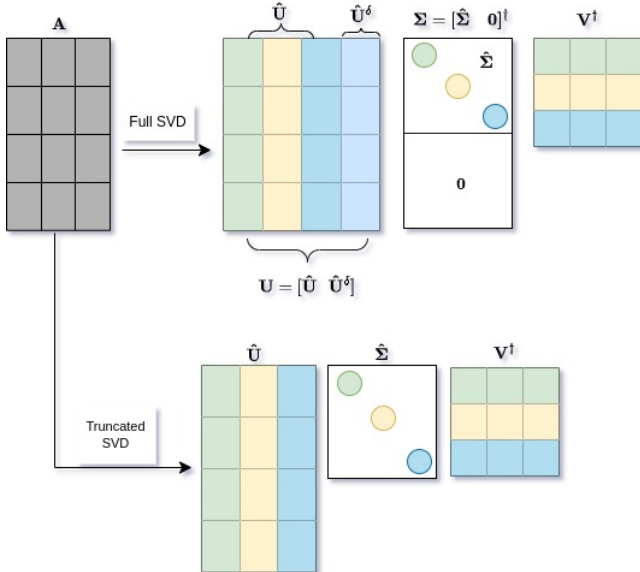


Fig. 6 A demonstration of full and truncated SVD. The columns of $\hat{\mathbf{U}}^\delta$ span a vector space that is complementary and orthogonal to that spanned by $\hat{\mathbf{U}}$ and $\hat{\Sigma}$ is an $m \times m$ diagonal matrix.

where Σ^w denotes the diagonal matrix of weighted singular values, which is obtained by scaling the diagonal matrix Σ with the weights

$$\Sigma_{jj}^w = \mathbf{W}_{jj} \Sigma_{jj}. \quad (17)$$

The decomposition solves the optimization problem:

$$\underset{\tilde{\mathbf{A}}, \text{ s.t. } \text{rank}(\tilde{\mathbf{A}})=r}{\text{argmin}} \|\mathbf{A} - \tilde{\mathbf{A}}\|_F = \mathbf{U} \Sigma^w \mathbf{V}^\dagger \quad (18)$$

Fig. 7 illustrates how the weighted SVD works. The choice of weights relies on the specific application. In image compression, for example, weights are assigned based on the importance of each pixel in the image. In other words, pixels with higher contrast may be given more weight than pixels with lower contrast.

Weighted SVD accurately captures the underlying structure of the data by weighting singular values according to their importance. This can be particularly beneficial in the case of noisy or incomplete data, as the algorithm can give more weight to reliable information. In addition, weighted SVD allows for better interpretability and control over the decomposition process, as particular singular values can be assigned a higher or lower priority based on domain knowledge. However, the computational cost of weighted SVD is generally higher than that of the traditional SVD due to the added complexity of handling weights. The weighted SVD introduces additional operations to

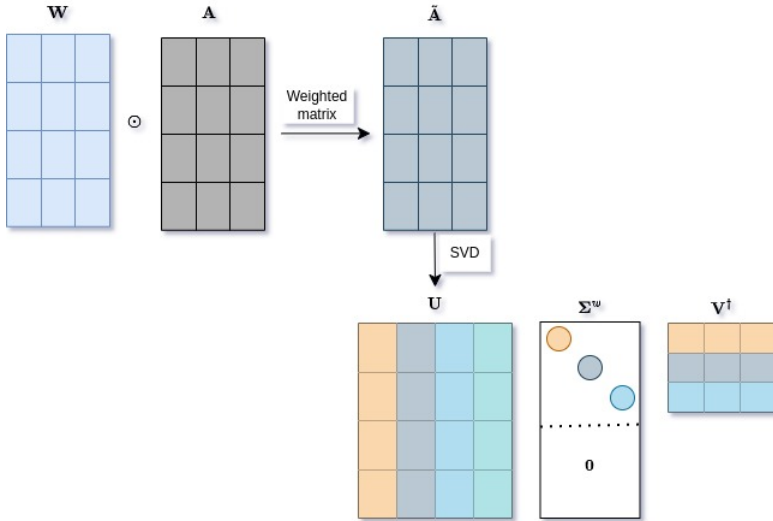


Fig. 7 A demonstration of weighted SVD.

account for the weights, which can lead to a higher time complexity depending on the specific implementation [184]. The memory requirement is the same as for truncated or full SVD, since $\mathbf{W}_{jj}\mathbf{\Sigma}_{jj}$ can be stored directly.

7.3 Randomized SVD

Randomized Singular Value Decomposition (rSVD) refers to a technique that approximates the SVD of a matrix using random projections [84]. The rSVD method has gained increasing popularity in recent years owing to its efficiency and scalability in large-scale data analysis [84, 185, 186]. In a general LRMA problem, the objective is to approximate the provided matrix \mathbf{A} using two smaller matrices, $\mathbf{B} \in \mathbb{C}^{m \times r}$ and $\mathbf{C} \in \mathbb{C}^{r \times n}$ with the conditions $r \ll n$ and $\mathbf{A} \approx \mathbf{BC}$. To achieve this approximation through rSVD, a two-stage computation was proposed by [84]. In the initial stage, a random projection matrix $\mathbf{P} \in \mathbb{C}^{n \times r}$ (with entries typically drawn from a standard normal or uniform distribution) is created to sample the column space of $\mathbf{A} \in \mathbb{C}^{m \times n}$, represented as:

$$\mathbf{Z} = \mathbf{AP}, \quad (19)$$

where $\mathbf{Z} \in \mathbb{C}^{m \times r}$ may be smaller than \mathbf{A} , especially for low-rank matrices with $r \ll n$. As a random projection matrix \mathbf{P} is unlikely to eliminate crucial components of \mathbf{A} , \mathbf{Z} serves as an accurate approximation of the column space of \mathbf{A} [187]. Consequently, the low-rank QR decomposition of \mathbf{Z} can be computed to obtain an orthonormal basis for \mathbf{A} :

$$\mathbf{Z} = \mathbf{QR}. \quad (20)$$

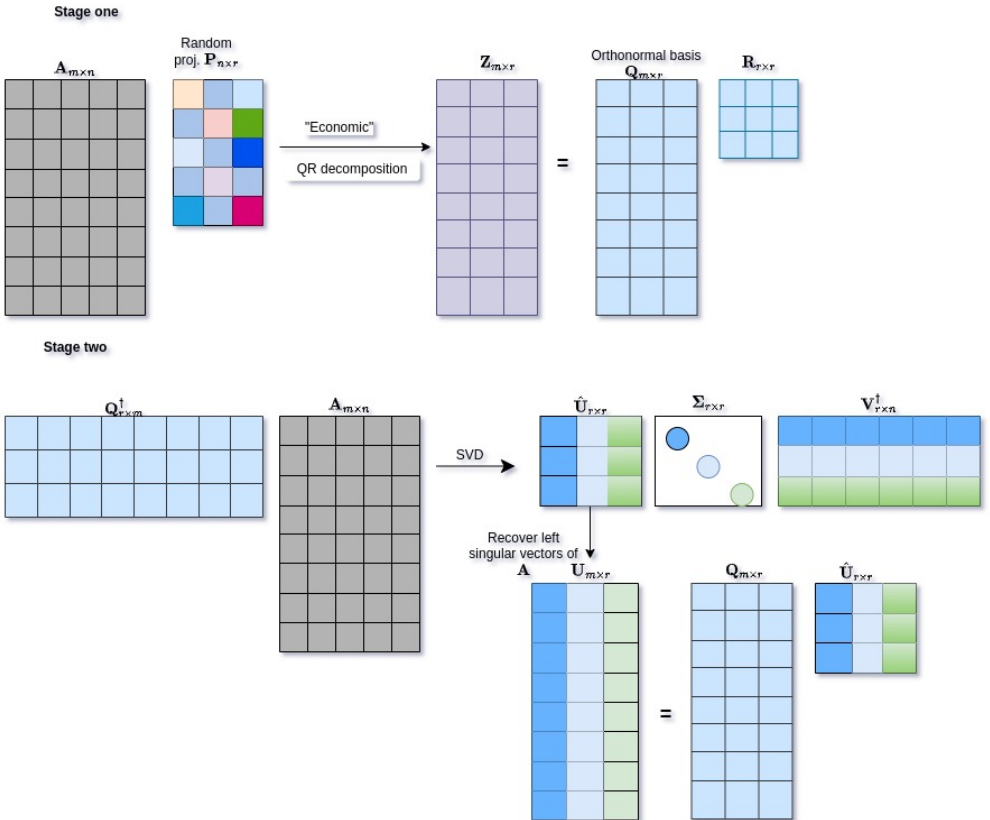


Fig. 8 A demonstration of random SVD.

In the second step, using the low-rank basis \mathbf{Q} , \mathbf{X} is projected into a smaller space, expressed as:

$$\mathbf{Y} = \mathbf{Q}^\dagger \mathbf{A}. \quad (21)$$

The SVD of \mathbf{Y} is given by:

$$\mathbf{Y} = \hat{\mathbf{U}} \Sigma \mathbf{V}^\dagger. \quad (22)$$

As \mathbf{Q} is orthonormal and approximates the column space of \mathbf{A} , the matrices Σ and \mathbf{V} are the same for both \mathbf{Y} and \mathbf{A} . The high-dimensional left singular vectors \mathbf{U} are reconstructed using $\hat{\mathbf{U}}$ and \mathbf{Q} :

$$\mathbf{U} = \mathbf{Q} \hat{\mathbf{U}}. \quad (23)$$

The rSVD algorithm is based on the idea that the matrix \mathbf{Q} acts as a randomized projection matrix, compressing the information in \mathbf{A} to a smaller

dimension, which is then used to compute the SVD of \mathbf{A} . The accuracy of the approximation depends on the number of columns, denoted as r , in the matrix \mathbf{Q} . A larger value of r leads to increased accuracy but also comes with higher computational cost. Fig. 8 demonstrates the steps in rSVD.

rSVD offers a computational advantage over traditional SVD by significantly reducing the time complexity associated with matrix factorization, especially for large datasets. The computational cost of rSVD is approximately given by $\mathcal{O}(mn \log(r))$ [84]. The logarithmic term ($\log(r)$) represents the number of iterations required for the power iteration method to converge to the desired number of singular values or components. In addition, rSVD has lower memory requirements, with a memory complexity of about $\mathcal{O}(mn + nr)$ [84, 188]. These attributes make rSVD highly scalable and efficient for applications with large amounts of data [84, 185, 186]. Moreover, due to the introduction of randomness, rSVD can provide higher robustness to outliers and noise, leading to more stable results in some instances. However, rSVD comes with certain limitations. It provides an approximate decomposition that may not achieve the same level of accuracy as the exact decomposition provided by traditional SVD. The need for parameter tuning, including selecting appropriate values for parameters such as the number of samples and the desired rank, may affect the approximation quality and must be carefully considered. It should also be noted that rSVD is best suited for tasks where an approximate decomposition is acceptable, such as dimensionality reduction. It may not be suitable for applications that require exact results.

7.4 Tensor SVD

The tensor SVD works by unfolding the tensor along one of its modes (i.e., dimensions), resulting in a tensor matrix representation [189]. The matrix SVD is then applied to this matrix representation to produce a set of orthogonal matrices and singular values. Let $\mathcal{A} \in \mathbb{C}^{I_1 \times I_2 \times \dots \times I_n}$ denotes a tensor of order n . The decomposition of a tensor, \mathcal{A} , is given by

$$\mathcal{A} = \mathcal{B} \times_1 \mathbf{U}^{(1)} \times_2 \mathbf{U}^{(2)} \times_3 \dots \times_n \mathbf{U}^{(n)}, \quad (24)$$

where \mathcal{B} is a core tensor of size (r_1, r_2, \dots, r_n) with rank r , and $\mathbf{U}^{(1)}, \mathbf{U}^{(2)}, \dots, \mathbf{U}^{(n)}$ are orthogonal matrices with size $I_1 \times r_1, I_2 \times r_2, \dots, I_n \times r_n$ respectively. The weights associated with each tensor component are stored in the core tensor \mathcal{B} , and the orthogonal matrices $\mathbf{U}^{(1)}, \mathbf{U}^{(2)}, \dots, \mathbf{U}^{(n)}$ represent the contribution of each mode to each component. The number of components is determined by r , which is typically much smaller than the tensor size. The components are recorded in descending order, with the first capturing the most variation in the tensor. Eq. 24 can be represented using a matrix form as

$$\mathcal{A} = \sum_{i_1=1}^{r_1} \sum_{i_2=1}^{r_2} \dots \sum_{i_n=1}^{r_n} b_{i_1, i_2, \dots, i_n} \mathbf{u}_{i_1}^{(1)} \otimes \mathbf{u}_{i_2}^{(2)} \dots \otimes \mathbf{u}_{i_n}^{(n)}, \quad (25)$$

where $\mathbf{u}_{i,j}^{(n)}$ denotes an i^{th} column of $\mathbf{U}^{(n)}$ and \otimes denotes the tensor product operation. If $b_{i_1, i_2, \dots, i_n} = 0$, that is, \mathcal{B} is diagonal then

$$\mathcal{A} = \sum_{i_1=1}^r b_{i_1 \dots i} \mathbf{u}_i^{(1)} \otimes \mathbf{u}_i^{(2)} \dots \otimes \mathbf{u}_i^{(n)} \quad (26)$$

except when $i_1 = i_2 = \dots = i_n$. The t-SVD is defined as

$$\mathcal{A} = \sum_{i_1=1}^r \xi_i \mathbf{u}_i^{(1)} \otimes \mathbf{u}_i^{(2)} \dots \otimes \mathbf{u}_i^{(n)}, \quad (27)$$

where ξ_i is the i^{th} singular value. Eq. 26 underlines the similarity between the t-SVD and the matrix SVD, where the singular values are replaced by tensors, and the factor matrices are replaced by vectors.

The t-SVD technique has both advantages and disadvantages in various applications. One of its notable advantages is its ability to reduce the dimensionality of multidimensional data, which is useful in compression, noise reduction, and feature extraction. This technique proves valuable in data analysis, as it helps uncover intricate patterns and relationships in complex datasets. However, tensor SVD also has drawbacks. As with any dimensionality reduction method, t-SVD can result in information loss since only the most significant singular values and vectors are preserved. While it can reveal patterns, their interpretation can be difficult, especially for high-dimensional tensors. In addition, the computational cost can be significant, especially for high-dimensional tensors, making it less practical for large datasets. The computational complexity of t-SVD in some typical tensor decomposing-based methods is about $\mathcal{O}(n^2m^2k + k^3)$, where n , m , and k denote the tensor dimensions [190].

7.5 Principal Component Analysis

Principal component analysis (PCA) is a mathematical technique used in data analysis and ML for dimensionality reduction and feature extraction. It identifies the most important features, or principal components, in the data matrix \mathbf{A} that capture the most significant variance. When reducing the number of feature variables in a dataset, reduced dimensionality trades accuracy for simplicity. Small datasets are easier to explore, visualize, and analyze with ML algorithms since they have few variables. Let \mathbf{x}_i denote the i^{th} column vector of the data matrix \mathbf{X} (denotes a covariance matrix of the centered variable) with n feature variables. A linear combination of \mathbf{x} 's is expressed as

$$\mathbf{t} = \sum_{i=1}^n w_i \mathbf{x}_i \quad (28)$$

$$= \mathbf{X}\mathbf{w}. \quad (29)$$

The objective is to find a set of orthogonal linear combinations of variables that capture the most variation in the data. That is,

$$\underset{\|\mathbf{w}\|=1}{\operatorname{argmax}} \operatorname{var}(\mathbf{Xw}). \quad (30)$$

To compute the first principal component, the first weight vector, $\mathbf{w}_{(1)}$, has to satisfy

$$\mathbf{w}_{(1)} = \underset{\|\mathbf{w}\|=1}{\operatorname{argmax}} \|\mathbf{Xw}\|^2 \quad (31)$$

$$= \underset{\|\mathbf{w}\|=1}{\operatorname{argmax}} (\mathbf{w}^\dagger \mathbf{X}^\dagger \mathbf{Xw}). \quad (32)$$

Since \mathbf{w} is a unit vector, Eq. 31 can be rewritten as

$$\mathbf{w}_{(1)} = \underset{\|\mathbf{w}\|=1}{\operatorname{argmax}} \left(\frac{\mathbf{w}^\dagger \mathbf{X}^\dagger \mathbf{Xw}}{\mathbf{w}^\dagger \mathbf{w}} \right). \quad (33)$$

To compute the k^{th} component, the $k-1$ principal components are subtracted from \mathbf{X} , that is

$$\tilde{\mathbf{X}}_k = \mathbf{X} - \sum_{j=1}^{k-1} \mathbf{Xw}_{(j)} \mathbf{w}_{(j)}^\dagger \quad (34)$$

and the weight vector that extracts maximum variance from $\tilde{\mathbf{X}}_k$ is given by

$$\mathbf{w}_{(k)} = \underset{\|\mathbf{w}\|=1}{\operatorname{argmax}} \|\tilde{\mathbf{X}}_k \mathbf{w}\|^2 \quad (35)$$

$$= \underset{\|\mathbf{w}\|=1}{\operatorname{argmax}} (\mathbf{w}^\dagger \tilde{\mathbf{X}}_k^\dagger \tilde{\mathbf{X}}_k \mathbf{w}). \quad (36)$$

Let \mathbf{W} denote a matrix containing the k selected eigenvectors as its columns, then the full principal component decomposition can be computed as

$$\mathbf{T} = \mathbf{XW}, \quad (37)$$

where \mathbf{T} is the matrix of principal components and each column represents a principal component. The resulting matrix \mathbf{T} contains the data's reduced-dimensional representation, capturing the most significant variation. The covariance matrix's eigenvectors and eigenvalues are critical in determining the directions and magnitudes of the principal components, respectively. Fig. 9 demonstrates the steps in PCA.

The main advantages of PCA include its ability to reduce the dimensionality of data while preserving important information, noise reduction, improve model performance, and visualize high-dimensional data. It is an unsupervised

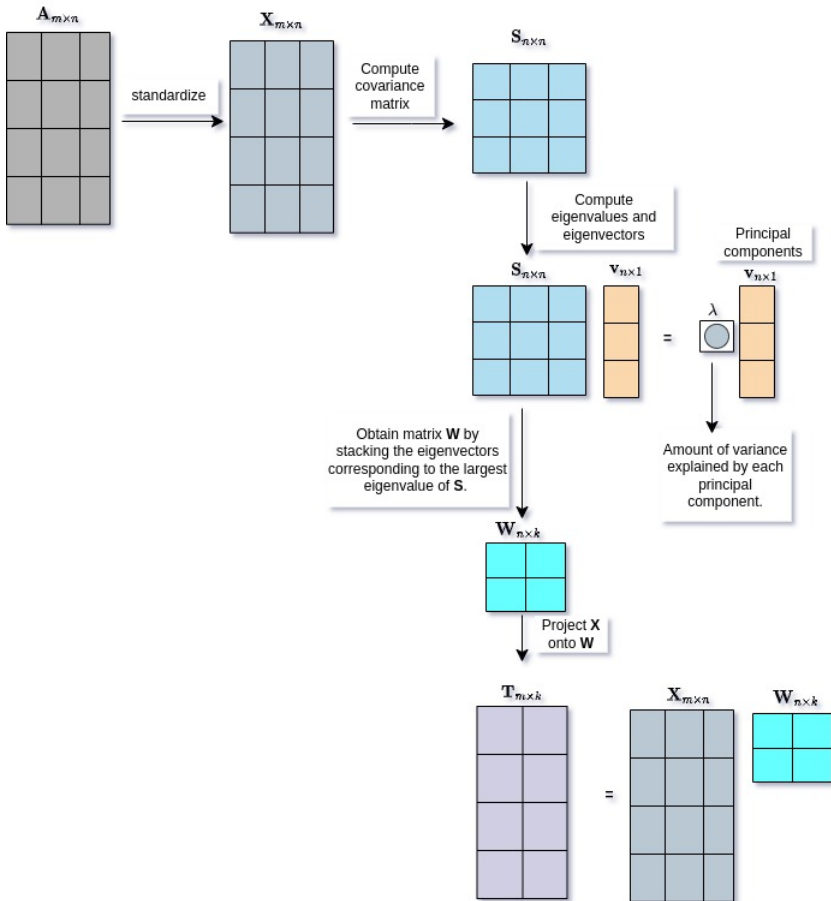


Fig. 9 A demonstration of PCA. In this example, k denotes the number of principal components to retain.

technique suitable for exploratory analysis. However, PCA assumes a linear data distribution and may not perform well with nonlinear relationships. It is also sensitive to outliers, as these can disproportionately affect the calculated principal components. In addition, interpretation of the transformed components can be challenging for complex datasets. The computation time for PCA is mainly influenced by the number of data points, m , and the number of features, n , in the dataset. The most time-consuming step is usually the eigenvalue decomposition or SVD, which has a computational complexity of $\mathcal{O}(n^3)$ for the covariance matrix and $\mathcal{O}(\min\{m^2n, mn^2\})$ for SVD [191, 192]. The memory requirement depends on the size of the covariance matrix or the SVD factor matrices. It is typically $\mathcal{O}(n^2)$ for the covariance matrix and $\mathcal{O}(\min\{m^2, mn\})$ for SVD [191, 192].

Table 15 provides a summary of various low-rank methods used in data analysis. It highlights their key strengths, weaknesses, and computational costs. The table is a valuable reference for selecting the most suitable low-rank method based on specific data analysis requirements.

Table 15 This table provides a detailed analysis of various low-rank methods, highlighting their respective strengths, weaknesses, computational cost, and compatibility with different data size constraints.

low-rank method	Strengths	Weakness	Computational cost
SVD	<ul style="list-style-type: none"> Provides an exact decomposition of the data matrix into orthogonal factors. Useful for dimensionality reduction, noise reduction, and feature extraction. 	<ul style="list-style-type: none"> Can be computationally expensive for large matrices. Sensitive to missing data and outliers. May not handle high-dimensional data well. 	<ul style="list-style-type: none"> Full SVD has time complexity of $\mathcal{O}(mn \min\{m, n\})$ and memory complexity of $\mathcal{O}(mn)$. While truncated SVD has time complexity $\mathcal{O}(mnr)$, and its memory complexity is $\mathcal{O}(mr + nr)$.
weighted SVD	<ul style="list-style-type: none"> Accurately captures the underlying structure of the data by weighting singular values according to their importance. Provides better interpretability and control over the decomposition process. 	<ul style="list-style-type: none"> Computational cost is generally higher than that of the traditional SVD. 	<ul style="list-style-type: none"> When $\mathbf{W}_{jj} \mathbf{\Sigma}_{jj}$ is stored directly, memory requirement is approximately $\mathcal{O}(mnr)$ or $\mathcal{O}(mn \min\{m, n\})$
rSVD	<ul style="list-style-type: none"> Faster than computing the full SVD for large matrices. Requires less memory than traditional SVD. Extract the most important features of a matrix while discarding noise and less significant components. 	<ul style="list-style-type: none"> SVD might not have clear interpretations as they would with the traditional SVD. Approximation might not be suitable for applications where high precision is crucial. 	<ul style="list-style-type: none"> Has time complexity of approximately $\mathcal{O}(mn \log(r))$ and a memory complexity of about $\mathcal{O}(mn + nr)$.
t-SVD	<ul style="list-style-type: none"> Suitable for multi-dimensional data, capturing interactions among multiple modes. Reduces the dimensionality of multidimensional data, which is useful in compression, noise reduction, and feature extraction 	<ul style="list-style-type: none"> Computational cost can be significant, especially for high-dimensional tensors Can result in information loss since only the most significant singular values and vectors are preserved. 	<ul style="list-style-type: none"> Complexity for full tensor SVD can be approximated as $\mathcal{O}(n^2 m^2 k + k^3)$.
PCA	<ul style="list-style-type: none"> Has the ability to reduce the dimensionality of data while preserving important information, noise reduction, improve model performance, and visualize high-dimensional data. 	<ul style="list-style-type: none"> Sensitive to scaling of features. It is not well suited for capturing nonlinear relationships in data. 	<ul style="list-style-type: none"> Has a computational complexity of $\mathcal{O}(n^3)$ for the covariance matrix and $\mathcal{O}(\min\{m^2 n, mn^2\})$ for SVD. Memory complexity is typically $\mathcal{O}(n^2)$ for the covariance matrix and $\mathcal{O}(\min\{m^2, mn\})$ for SVD.

8 Findings and Discussion

This section addresses the findings and drawbacks that arise from the review. We also provide valuable insights and recommendations for possible future directions in this area of study. Fig. 10 summarizes the findings of this study. The figure shows the low-rank method used in the reviewed publications used while performing various tasks on the medical data. It also highlights the different types that were used. In terms of the LLRMA approximation, the figure shows the similarity measurement methods used in the studied publications during the matching phase.

8.1 High Rate of LLRMA Applied from 2015

From the reviewed papers, LLRMA has shown the potential and ability to capture the underlying structure of data while reducing its dimensionality with little to no feature loss or distortion due to the locality coherence search. This approach balances data compression and detail preservation by exploiting the local low-rank property. The local nature of the approximation allows for localized analysis, where specific regions or patches of the data can be accurately represented, leading to improved performance in tasks such as image processing and computer vision [193]. Moreover, LLRMA exhibits robustness to outliers [194], which enhances its applicability in real-world scenarios where noisy or corrupted data may be present. This robustness ensures that the approximation remains accurate and reliable, even in the presence of abnormalities. Additionally, LLRMA provides a denoising capability, separating the essential signal from noise and improving the quality of the data representation [124, 125, 127, 129, 135, 150]. Its effectiveness in preserving meaningful information while reducing computational complexity and memory usage makes LLRMA a powerful tool in various domains, including medical image analysis as studied in this paper.

It is important to note that LLRMA was originally introduced in 2013, but its use in the medical field began in 2015. This information is key to understanding the use of the LLRMA approximation in the medical field. Fig. 11 shows that there is no documented use of LLRMA prior to 2015. However, there was a significant change after 2015, when researchers in the medical field began to apply the LLRMA technique. During this period, we found that of the total 40 papers published in the medical field between 2015 and 2023, only 12 papers applied LRMA, while 28 papers used LLRMA techniques. Fig. 12 also shows that a more significant proportion of publications from 2015 to 2023 focused on the LLRMA approximation compared to the LRMA approximation, i.e., 31% of publications used the LRMA approximation, while 69% used the LLRMA approximation. This trend highlights a notable shift in research preferences and the crucial role that the LLRMA approximation plays in the medical field.

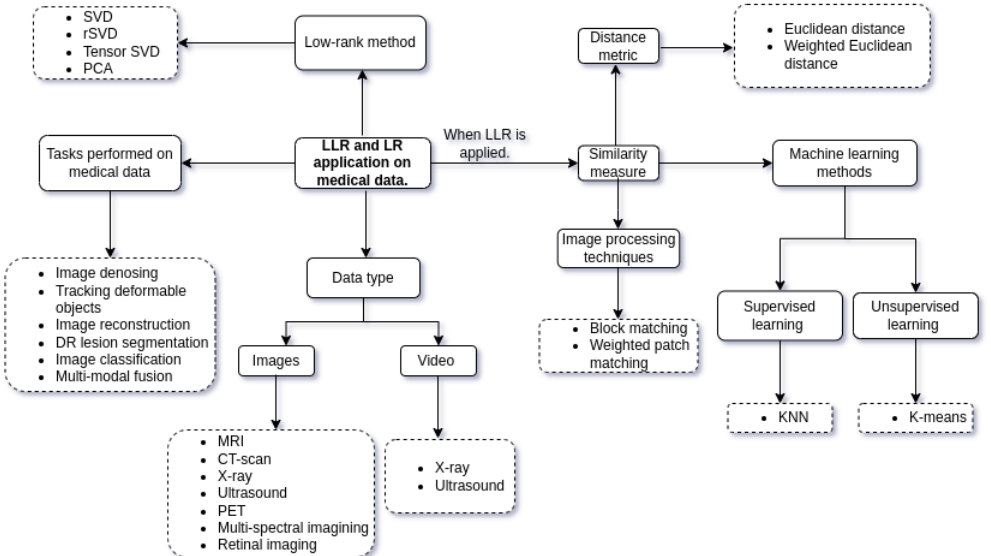


Fig. 10 An overview of the application of LLRMA and LRMA to medical data.

8.2 Shallow Similarity Methods

The reviewed papers utilized different similarity measures (as shown in Fig. 10 and discussed in Section 6) such as distance metrics (i.e., Euclidean distance [124, 126, 131, 136, 137, 140–144, 148] and weighted Euclidean [72]), shallow learning models (i.e., KNN [73, 123, 129, 135, 147] and k-means [134]) and image processing techniques (i.e., blocking matching [125, 127, 130, 132, 133, 140] and weighted patch matching [139]) during the patch-matching stage to measure similar patches. These models are simple but effective techniques commonly used in different of machine-learning tasks. The use of shallow models in the papers under review indicates a preference for simplicity, interpretability, and computationally efficient techniques. These models provide simple and understandable solutions to a variety of machine-learning problems.

While the above models are valuable techniques for measuring patch similarity, they also have certain limitations. For instance, Euclidean and weighted Euclidean distances are sensitive to the scale and range of the input features. If the features have different scales, this can lead to biased distance calculations and inaccurate similarity measurements. Normalizing the features can help mitigate this problem but may not always be sufficient for very heterogeneous data. KNN suffers from the curse of dimensionality, where performance decreases as the number of dimensions or features increases. In high-dimensional spaces, nearest neighbors may not provide accurate similarity estimates, resulting in lower performance. In addition, it can be challenging to determine the appropriate value of k , as a small k can lead to noisy decisions, while a large k can over-smooth local patterns. K-means is sensitive to the

choice of initial cluster centroids and may converge to suboptimal solutions. The method also reaches its limits for non-uniformly sized or non-spherical clusters, as it assumes the same variance and spherical shape for all clusters. For complex medical image data, these assumptions may not hold, resulting in suboptimal cluster assignments and inaccurate similarity measurements. Block matching lacks fine-grained detail because it divides an image into fixed-size blocks, potentially missing subtle texture or structure variations that may exist within those blocks. This can lead to a loss of sensitivity to local variations, resulting in a coarse representation of the image content. Another significant drawback of block matching is its sensitivity to block size and placement. The choice of block size is critical because smaller blocks capture finer details but increase computational complexity, while larger blocks may miss crucial local information. On the other hand, weighted patch matching is sensitive to small variations in lighting, noise, or texture, which can cause patches to be classified as dissimilar even though they represent similar objects or structures. Additionally, it lacks a deep semantic understanding of the content within patches, making it unable to distinguish between patches with similar textures but different underlying objects or concepts.

The applicability of these shallow similarity checks is dependent on the specific problem and dataset characteristics. In some cases, more complex or deep learning (DL) models may be required to capture intricate patterns or achieve higher performance. In areas such as self-driving cars, for example, the complexity of processing large amounts of sensor data from cameras, lidar, and radar makes shallow methods for similarity measuring insufficient [195, 196]. DL models such as convolutional neural networks (CNNs) and recurrent neural networks (RNNs) are remarkable for learning complex spatial and temporal features from raw sensor data, making them essential for self-driving systems [197]. Similarly, natural language processing (NLP) is another area where DL has made a significant impact. Tasks such as document similarity, sentiment analysis, and machine translation often require the analysis of large and complex textual data [198]. DL models, including transformers and BERT, have revolutionized NLP by enabling models to learn complicated patterns and relationships in text data [199, 200]. In these domains, the complexity and dimensionality of the data, as well as the need to capture complex patterns, make shallow model similarity checks inadequate. DL models have been shown to be more adaptable and effective, as they can automatically learn relevant features and relationships from data [201, 202]. As a result, researchers and practitioners in these domains are increasingly relying on DL for similarity and pattern recognition tasks [203, 204]. The shallow similarity methods discussed in this section would fail in these fields due to complexity, and only DL methods can adapt. The medical field is growing with a huge amount of data being collected and therefore might reach the stage where these shallow methods won't work anymore, therefore, this requires urgent investigation for DL methods in similarity check in medical image analysis

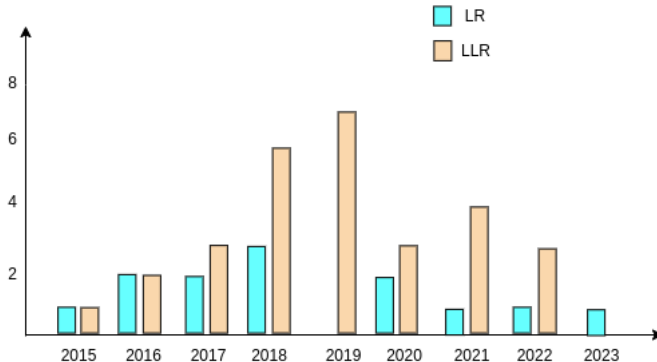


Fig. 11 Number of publications that applied LRMA or LLRMA technique on medical images.

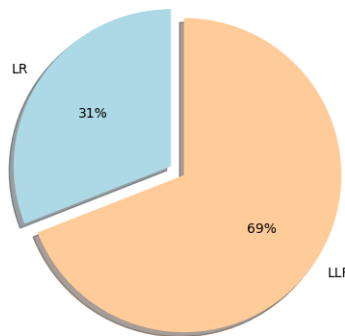


Fig. 12 A pie chart showing the distribution of publications using LLRMA and LRMA.

8.3 Data Type

The ability to handle and analyze different data modalities in healthcare is crucial due to the variety of information generated and collected in the medical field. Each data modality offers unique insights, but deriving meaningful insights from these modalities requires advanced technologies and methodologies. Advances in NLP, ML, and artificial intelligence (AI) have led to the development of techniques that can process, extract, and make sense of information from all three types of medical data (i.e., structured, semi-structured and unstructured data) to enable more comprehensive and informed healthcare decision making. For example, NLP can be used to extract diagnoses, treatments, and patient outcomes from physician notes, enabling better data integration and analysis [205, 206]. In contrast, ML techniques can be used to identify patterns, correlations, and anomalies in structured and semi-structured data [207, 208]. For example, ML algorithms can learn from historical patient data to predict disease advancement, suggest treatment options, or detect potential damaging events based on structured data. On the

other hand, AI models can be used to process and analyze medical data across modalities [209, 210]. For example, image recognition using DL algorithms can help analyze medical images to detect signs of disease. AI-driven decisions can help healthcare professionals make more informed treatment decisions by analyzing a combination of structured and unstructured data. In Sections 8.3.1, 8.3.2, and 8.3.3 we discuss various data modalities not considered in the reviewed papers (Fig. 10 shows unstructured modality that was considered in the reviewed publications). We also discuss whether it is possible to apply the LLRMA approximation technique to other modalities, such as structured and semi-structured.

8.3.1 Structured Data

Structured data in healthcare refers to information that is organized and formatted in a consistent and predefined way so that it can be easily managed, accessed, and analyzed [211]. Examples of structured data were not included in the publications reviewed include electronic health records (i.e., contain structured data such as patient demographics, medical history, medications, allergies, laboratory results, and clinical notes) and medical test result can be recorded in the form of a numeric or boolean value [212].

The LRMA matrix approximation technique can be applied to patient demographic data to analyze and extract insights from complex healthcare data. For example, if we have a comprehensive patient demographic dataset with various features (i.e., age, gender, ethnicity, medical history, and more), the study's goal is to reduce the dimensionality of the patient demographic dataset to visualize and cluster it. By representing the data as a matrix and applying matrix factorization, such as SVD, dimensionality can be effectively reduced while retaining the most important information. This facilitates the visualization of patient profiles in lower dimensions and makes it easier to identify patient clusters with similar demographic characteristics. These clusters can help healthcare professionals to understand similar patient characteristics better and adapt their services accordingly. The feasibility of this study depends on the availability of a sufficiently large and high-quality patient demographic dataset, as well as the privacy and ethical considerations associated with handling patient data.

8.3.2 Semi-structured Data

Semi-structured data in healthcare refers to information that falls between fully structured and fully unstructured data [213]. They exhibit some form of organization but allow for more flexibility and variability compared to strictly structured data. Semi-structured data retains certain structural elements, such as predefined data fields or tags, while being able to accommodate different content and formats. Examples of semi-structured data that were not included in the publications reviewed include clinical forms (i.e., healthcare facilities use electronic forms for data collection that may allow free-text entries such as

symptoms and medical history), radiology and laboratory reports (i.e., comments made by healthcare professionals), patient history summaries (i.e., may include information about the patient's current condition and treatment plan), medical literature, transcribed voice notes (i.e., healthcare providers may dictate notes during patient visits), and patient questionnaires (i.e., may include open-ended questions to collect patient feedback and information). TheLRMA technique can be applied to a semi-structured dataset, for example, if a medical institution issues a patient satisfaction questionnaire that contains both open-ended questions and rating scales. The questionnaire may include questions on the quality of medical care, communication with healthcare providers and general satisfaction. Patients provide ratings on a scale of 1 to 5 for certain aspects and provide open-ended responses to capture additional feedback. To convert this questionnaire data into a matrix, a table in which each row corresponds to a patient and each column represents a specific question or rating category can be created, as shown in Fig. 13. The open-ended responses can be pre-processed by creating a document term matrix (DTM). ALRMA technique (e.g., PCA) can then be applied to the resulting matrix for feature reduction, especially if there are a large number of questions, making subsequent analyses more manageable.

8.3.3 Unstructured Data

Unstructured healthcare data refers to information that does not follow a pre-defined and organized format, making it more difficult to manage, analyze, and interpret compared to structured data [211]. Examples of unstructured data that were not included in the publications reviewed include clinical notes (i.e., details of a patient's medical history, symptoms, physical examinations and treatment plans), pathology reports (i.e., information about tissue samples and biopsies), handwritten documents (i.e., patient charts, prescriptions and other medical documents that are handwritten), audio recordings (i.e., dictated notes, voice memos, speech therapy sessions, lung sounds, recordings of heartbeats and audio recordings of patient conversations or surgical procedures that may contain valuable medical information), social media content and comments (i.e., patients may share their health experiences and ask for advice on social media platforms and online forums), and faxed versions of structured data (i.e., structured prescription data, when faxed to a pharmacy, loses its format and becomes an unstructured data) [212]. TheLRMA method is primarily used for image data and may not be directly applicable to audio data since audio data as a one-dimensional signal may not exhibit the same low-rank properties [214]. The concept ofLRMA assumes that the data can be represented by a low-dimensional subspace, which aligns well with the structure of images [86]. However, clinical notes, pathology reports, handwritten documents, and comments faxed versions of structured data may not have the same low-rank properties thatLRMA techniques can exploit [215]. In the context of social media content, latent semantic analysis (LSA) can be used to obtain a low-rank matrix approximation to discover underlying semantic

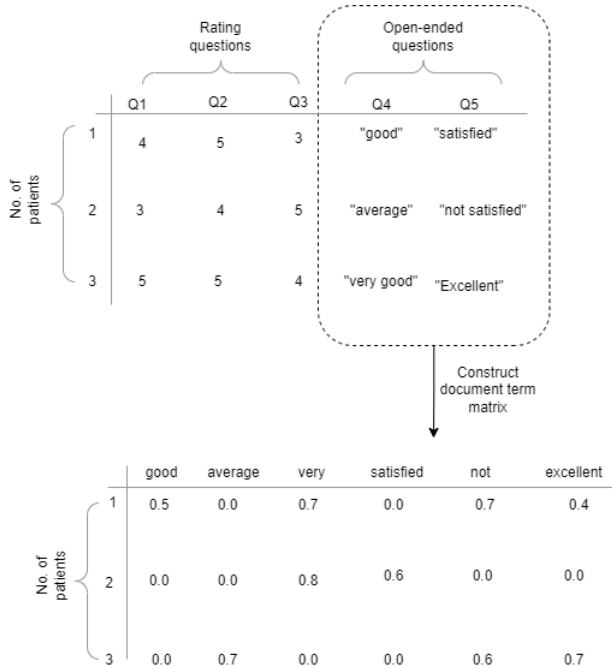


Fig. 13 A demonstration of how a numeric matrix is constructed from a questionnaire with open-ended questions. In the DTM, each column represents a unique term or word that appears in the open-ended responses. These terms were processed and converted into a numerical representation using the frequency-inverse document frequency (TF-IDF). The numerical values in the DTM represent the TF-IDF weights for each term in each patient's response. TF-IDF evaluates how important a word is for a document (in this case, a patient's response) compared to a collection of documents (all patient responses). A higher TF-IDF value indicates a higher importance of the term in that specific response. For example, if patient 1 has higher TF-IDF values for terms such as *Good*, *Satisfied* and *Great*, this means that these terms are more important in describing patient 1's response.

patterns in a large collection of posts. For example, a dataset may consist of thousands of tweets. Each tweet can be considered as a document, and the words in these tweets form the terms. By constructing DTM, where rows represent tweets (i.e., number of tweets) and columns represent terms (i.e., words), a high-dimensional matrix is created that encodes the frequency of each word in each tweet. LSA reduces the dimensionality of this matrix by performing SVD, which helps to capture the latent semantic relations between terms and documents.

8.4 Applicable Only on Regular Data-type

The LRMA technique is useful in data analysis and dimensionality reduction, especially for regular data types such as matrices and tensors. However, it may not be directly applicable to irregular data types such as triangular matrices or irregularly distributed data points. The main reason for this limitation is that

low-rank methods assume that the data can be well approximated by a low-dimensional subspace. Irregular data often violate this assumption since it may lack consistent patterns due to their unpredictable nature. This makes it challenging to identify a small set of underlying factors that can effectively capture the variation in the data. In the context of regular data with missing entries, techniques such as inpainting are used to fill in the missing values before applying low-rank methods. Inpainting is a process of estimating missing values based on the available data and certain assumptions about the underlying structure of the data. While inpainting can be effective, it comes with computational complexity and possible inaccuracies in prediction. Inpainting quality is critical when low-rank methods are used for data with missing entries. If the missing entries are not predicted accurately, it can significantly affect the performance of the LRMA. Inaccurate inpainting can introduce errors in the estimated low-rank structure, resulting in a poor representation of the original data.

8.5 Effect of Patch Size in Medical Images

When an image is divided into patches, the amount of local information captured in each patch is determined by the size of the patch. Smaller patch sizes are more focused on capturing fine details and local variations within a given region of interest. The ML algorithm can look more closely at smaller structures or subtle anomalies in a medical image by using smaller patches. This allows the algorithm to analyze localized patterns, textures, edges, or other specific features that may be required for accurate analysis. Smaller image patches can be useful in medical imaging, for example, to detect small lesions or specific anatomical structures that require a high level of detail. By analyzing smaller patches, the algorithm can better capture complex patterns that may go unnoticed in larger patches. Larger patch sizes, on the other hand, cover a broader context and capture more surrounding information in addition to the target region. This broader context provides a higher-level perspective and allows the algorithm to detect spatial relationships or global patterns in the image. Larger patches can assist in the analysis of larger structures or in capturing the overall layout of anatomical regions. Larger patch sizes in medical images can be useful for tasks like organ segmentation or classification, where the spatial arrangement of structures or the overall context is critical. The algorithm can achieve a better understanding of global features and relationships among different regions by incorporating more contextual information.

The patch size chosen is determined by the scale and nature of the features or anomalies that the algorithm must detect or analyze. It is critical for the algorithm's performance and ability to extract meaningful information from medical images to strike a balance between capturing fine local details and incorporating sufficient contextual information. In the studied works, the patch sizes were varied depending on the noise level, i.e., with increasing noise, the patch size was increased [126, 130, 136, 140, 141]. In contrast, [145] varied patch size depending on the dimensions. Some authors [131, 143, 146, 148] compared

different patch sizes and selected the one that provided optimal results. While others [72, 73, 124, 125, 129, 132, 133, 137, 138, 140, 144, 147] did not compare different patch sizes.

To mitigate the effects of patch size, random search (RS) can be used in future studies to find the optimal patch size. RS is a valuable approach for hyper-parameter tuning, model selection, and optimization tasks because it provides a simple and effective way to explore the parameter space and determine appropriate parameter configurations for a given problem. In the analysis of medical images, such as MRI, CT scans, or ultrasound, the choice of patch size can significantly affect the performance of various tasks, such as segmentation, denoising or classification. The patch size determines the spatial context of the algorithm and can influence local and global feature extraction. By applying RS, one can systematically evaluate different patch sizes by drawing a random sample from a predefined range. In this approach, a patch size is selected, the algorithm is trained and evaluated with that patch size, and then the process is repeated with a different patch size. Depending on the task, the evaluation can be based on predefined performance metrics such as accuracy. The feasibility of RS in selecting the optimal patch size depends on several considerations. The size of the search space and the granularity of the patch size range are critical factors. If the search space is small or the range is well-defined, the RS can effectively cover the space with a reasonable number of iterations. However, in cases where the search space is large or the range is not well constrained, RS may require many iterations to sufficiently explore the space, making it less feasible. In addition, the computational cost of evaluating the algorithm for each patch size can impact feasibility. A hybrid approach can be used to improve feasibility. RS can be combined with other optimization techniques, such as Bayesian optimization, to leverage their strengths and overcome the limitations of RS. This hybrid approach enables more targeted exploration and can potentially increase efficiency in finding the optimal patch size.

9 Conclusion

All publications included in this study used shallow models to measure the similarity between patches. The drawbacks of these techniques are discussed in detail in Section 8.2. In future work, DL methods such as DeepLab can be used to improve the effectiveness of these proposed methods. DeepLab is a DL-based semantic segmentation model used for image analysis tasks. It is primarily used to assign class labels to each pixel in an image to identify different objects and regions within the image [117]. DeepLab is not explicitly used to measure similar patches but can be used to measure similar patches by extracting meaningful features and capturing the underlying semantic information within the patches. The process begins by extracting patches from the input image and isolating regions of interest. Then, a pre-trained DeepLab model that has learned to recognize different objects and regions is applied to

these patches to create pixel-level semantic segmentation masks. These masks assign class labels to individual pixels, effectively outlining different objects and structures within the patches. The semantic segmentation masks can be used to define a similarity measure for comparing the patches. Intersection over union (IoU) is a commonly used similarity measure that quantifies the overlap between two masks [216]. The degree of similarity can be determined by calculating the IoU values between pairs of patches. Setting an IoU threshold allows the classification of patches as similar or dissimilar. Patches that exceed the threshold are considered similar, while patches that fall below are considered dissimilar. DeepLab ensures that the underlying patterns and structures within the patches are captured, providing valuable context for the similarity measurement process. Since DeepLab has been trained on a diverse dataset, it can effectively recognize complex objects and regions, making it ideal for scenarios where patches contain complicated information. The feasibility of using DeepLab to measure similar patches depends on several factors. The computational complexity of DeepLab could be a concern for applications that require real-time performance or efficient processing, as it is a deep neural network that requires significant computational resources. In addition, training DeepLab requires a large dataset with pixel-level annotations, making it less suitable for tasks with limited or dissimilar training data. Choosing an appropriate similarity threshold is critical to avoid false positives or missing relevant similarities. The choice of patch size can also impact the effectiveness of the method, as small patches may lose large-scale similarities and large patches may lose fine-grained details. Overall, the suitability of DeepLab depends on the application domain and whether semantic information is critical to the task.

In conclusion, there has been a remarkable shift towards LLRMA in medical research since 2015, highlighting the efficiency of this method in capturing complex structures in medical data. Although shallow similarity methods are widely used, they have limitations in dealing with the increasing complexity of healthcare data. Therefore, it is recommended that advanced techniques such as DeepLab be explored for improved similarity measurement. This work also emphasizes the importance of applying LRMA to different healthcare data modalities and suggests using RS for optimal patch size for medical image analysis in future studies.

Acknowledgments

This work is based on the research supported in part by the National Research Foundation of South Africa (Ref Numbers CSRP23040990793). C.N. thanks the Australian Research Council Centre of Excellence for All Sky Astrophysics in 3 Dimensions (ASTRO 3D) for support through project number CE170100013. S. H., M. A. and J. B. thank Rhodes University for financial support.

Data Availability Statement

The datasets used and/or analysed during the current study are available from the corresponding author on reasonable request.

References

- [1] Hussain, S., Mubeen, I., Ullah, N., Shah, S.S.U.D., Khan, B.A., Zahoor, M., Ullah, R., Khan, F.A., Sultan, M.A.: Modern diagnostic imaging technique applications and risk factors in the medical field: A review. *BioMed Research International* **2022** (2022)
- [2] Umar, A., Atabo, S.: A review of imaging techniques in scientific research/clinical diagnosis. *MOJ Anat Physiol* **6**(5), 175–83 (2019)
- [3] Ganguly, D., Chakraborty, S., Balitanas, M., Kim, T.-h.: Medical imaging: A review. In: International Conference on Security-Enriched Urban Computing and Smart Grid, pp. 504–516 (2010). Springer
- [4] Shah, N., Bansal, N., Logani, A.: Recent advances in imaging technologies in dentistry. *World journal of radiology* **6**(10), 794 (2014)
- [5] Lieberman, I.H., Togawa, D., Kayanja, M.M., Reinhardt, M.K., Friedlander, A., Knoller, N., Benzel, E.C.: Bone-mounted miniature robotic guidance for pedicle screw and translaminar facet screw placement: Part i—technical development and a test case result. *Neurosurgery* **59**(3), 641–650 (2006)
- [6] Islam, S., Nasim, M., Hossain, I., Ullah, D.M.A., Gupta, D.K.D., Bhuiyan, M.M.H.: Introduction of medical imaging modalities. *arXiv preprint arXiv:2306.01022* (2023)
- [7] Tavazzi, E., Zivadinov, R., Dwyer, M.G., Jakimovski, D., Singhal, T., Weinstock-Guttman, B., Bergsland, N.: Mri biomarkers of disease progression and conversion to secondary-progressive multiple sclerosis. *Expert Review of Neurotherapeutics* **20**(8), 821–834 (2020)
- [8] Delorme, S., Baur-Melnyk, A.: Imaging in multiple myeloma. *European journal of radiology* **70**(3), 401–408 (2009)
- [9] Chin, E.J., Chan, C.H., Mortazavi, R., Anderson, C.L., Kahn, C.A., Summers, S., Fox, J.C.: A pilot study examining the viability of a pre-hospital assessment with ultrasound for emergencies (pause) protocol. *The Journal of emergency medicine* **44**(1), 142–149 (2013)
- [10] Tayal, V.S., Graf, C.D., Gibbs, M.A.: Prospective study of accuracy and outcome of emergency ultrasound for abdominal aortic aneurysm over

two years. *Academic Emergency Medicine* **10**(8), 867–871 (2003)

- [11] Aerts, H.J.: The potential of radiomic-based phenotyping in precision medicine: a review. *JAMA oncology* **2**(12), 1636–1642 (2016)
- [12] MacEachern, S.J., Forkert, N.D.: Machine learning for precision medicine. *Genome* **64**(4), 416–425 (2021)
- [13] Pinker, K., Chin, J., Melsaether, A.N., Morris, E.A., Moy, L.: Precision medicine and radiogenomics in breast cancer: new approaches toward diagnosis and treatment. *Radiology* **287**(3), 732–747 (2018)
- [14] Li, Z., Zhang, X., Müller, H., Zhang, S.: Large-scale retrieval for medical image analytics: A comprehensive review. *Medical image analysis* **43**, 66–84 (2018)
- [15] Panayides, A.S., Amini, A., Filipovic, N.D., Sharma, A., Tsafaris, S.A., Young, A., Foran, D., Do, N., Golemati, S., Kurc, T., *et al.*: Ai in medical imaging informatics: current challenges and future directions. *IEEE journal of biomedical and health informatics* **24**(7), 1837–1857 (2020)
- [16] Yu, H., Yang, L.T., Zhang, Q., Armstrong, D., Deen, M.J.: Convolutional neural networks for medical image analysis: state-of-the-art, comparisons, improvement and perspectives. *Neurocomputing* **444**, 92–110 (2021)
- [17] Bolón-Canedo, V., Sánchez-Marcano, N., Alonso-Betanzos, A.: Feature selection for high-dimensional data. *Progress in Artificial Intelligence* **5**, 65–75 (2016)
- [18] Lee, C.H., Yoon, H.-J.: Medical big data: promise and challenges. *Kidney research and clinical practice* **36**(1), 3 (2017)
- [19] Shinde, B., Dani, A.: Noise detection and removal filtering techniques in medical images. *Int J Eng Res Appl* **2**(4), 311–6 (2012)
- [20] Na, Y., Zhao, L., Yang, Y., Ren, M.: Guided filter-based images fusion algorithm for ct and mri medical images. *IET Image Processing* **12**(1), 138–148 (2018)
- [21] Kumar, N., Nachamai, M.: Noise removal and filtering techniques used in medical images. *Orient. J. Comput. Sci. Technol* **10**(1), 103–113 (2017)
- [22] Ilango, G., Marudhachalam, R.: New hybrid filtering techniques for removal of gaussian noise from medical images. *ARPN Journal of Engineering and Applied Sciences* **6**(2), 8–12 (2011)
- [23] Bhonsle, D., Chandra, V., Sinha, G.: Medical image denoising using

bilateral filter. International Journal of Image, Graphics and Signal Processing **4**(6), 36 (2012)

- [24] Gravel, P., Beaudoin, G., De Guise, J.A.: A method for modeling noise in medical images. IEEE Transactions on medical imaging **23**(10), 1221–1232 (2004)
- [25] Naimi, H., Adamou-Mitiche, A.B.H., Mitiche, L.: Medical image denoising using dual tree complex thresholding wavelet transform and wiener filter. Journal of King Saud University-Computer and Information Sciences **27**(1), 40–45 (2015)
- [26] Devadoss, C.P., Sankaragomathi, B.: Near lossless medical image compression using block bwt–mtf and hybrid fractal compression techniques. Cluster Computing **22**, 12929–12937 (2019)
- [27] Sudha, V., Sudhakar, R.: Two dimensional medical image compression techniques-a survey. ICGST-GVIP Journal **11**(1), 9–20 (2011)
- [28] Liu, S., Bai, W., Zeng, N., Wang, S.: A fast fractal based compression for mri images. Ieee Access **7**, 62412–62420 (2019)
- [29] Anandan, P., Sabeenian, R.: Medical image compression using wrapping based fast discrete curvelet transform and arithmetic coding. Circuits and Systems **7**(8), 2059–2069 (2016)
- [30] Jones, P.W., Daly, S.J., Gaborski, R.S., Rabbani, M.: Comparative study of wavelet and discrete cosine transform (dct) decompositions with equivalent quantization and encoding strategies for medical images. In: Medical Imaging 1995: Image Display, vol. 2431, pp. 571–582 (1995). SPIE
- [31] Wu, Y.-G., Tai, S.-C.: Medical image compression by discrete cosine transform spectral similarity strategy. IEEE Transactions on Information Technology in Biomedicine **5**(3), 236–243 (2001)
- [32] Kaur, K., Malhotra, S.: Image compression using haar wavelet transform and discrete cosine transform. International Journal of Computer Applications **125**(11) (2015)
- [33] Singh, A.K., Kumar, B., Dave, M., Mohan, A.: Multiple watermarking on medical images using selective discrete wavelet transform coefficients. Journal of Medical Imaging and Health Informatics **5**(3), 607–614 (2015)
- [34] Devassy, B.M., George, S.: Dimensionality reduction and visualisation of hyperspectral ink data using t-sne. Forensic science international **311**, 110194 (2020)

- [35] Bibal, A., Vu, V.M., Nanfack, G., Frénay, B.: Explaining t-sne embeddings locally by adapting lime. In: 28th European Symposium on Artificial Neural Networks, Computational Intelligence and Machine Learning: ESANN2020, pp. 393–398 (2020). ESANN (i6doc. com)
- [36] Faust, K., Xie, Q., Han, D., Goyle, K., Volynskaya, Z., Djuric, U., Diamandis, P.: Visualizing histopathologic deep learning classification and anomaly detection using nonlinear feature space dimensionality reduction. *BMC bioinformatics* **19**, 1–15 (2018)
- [37] Jamieson, A.R., Giger, M.L., Drukker, K., Li, H., Yuan, Y., Bhooshan, N.: Exploring nonlinear feature space dimension reduction and data representation in breast cadx with laplacian eigenmaps and-sne. *Medical physics* **37**(1), 339–351 (2010)
- [38] Jin, F., Fieguth, P., Winger, L., Jernigan, E.: Adaptive wiener filtering of noisy images and image sequences. In: Proceedings 2003 International Conference on Image Processing (Cat. No. 03CH37429), vol. 3, p. 349 (2003). IEEE
- [39] Milanfar, P.: Symmetrizing smoothing filters. *SIAM Journal on Imaging Sciences* **6**(1), 263–284 (2013)
- [40] Doymaz, F., Bakhtazad, A., Romagnoli, J.A., Palazoglu, A.: Wavelet-based robust filtering of process data. *Computers & Chemical Engineering* **25**(11-12), 1549–1559 (2001)
- [41] Rahman, S.M., Hasan, M.K.: Wavelet-domain iterative center weighted median filter for image denoising. *Signal Processing* **83**(5), 1001–1012 (2003)
- [42] Pradhan, A., Pati, N., Rup, S., Panda, A.S., Kanoje, L.K.: A comparative analysis of compression techniques—the sparse coding and bwt. *Procedia Computer Science* **92**, 106–111 (2016)
- [43] Toufik, B., Mokhtar, N.: The wavelet transform for image processing applications. *Advances in Wavelet Theory and Their Applications in Engineering, Physics and Technology* **17**, 395–422 (2012)
- [44] Xiang, Z., Xu, H., Ramadge, P.J.: Learning sparse representations of high dimensional data on large scale dictionaries. *Advances in neural information processing systems* **24** (2011)
- [45] Zheng, M., Bu, J., Chen, C., Wang, C., Zhang, L., Qiu, G., Cai, D.: Graph regularized sparse coding for image representation. *IEEE transactions on image processing* **20**(5), 1327–1336 (2010)

- [46] Van der Maaten, L., Hinton, G.: Visualizing data using t-sne. *Journal of machine learning research* **9**(11) (2008)
- [47] Gisbrecht, A., Schulz, A., Hammer, B.: Parametric nonlinear dimensionality reduction using kernel t-sne. *Neurocomputing* **147**, 71–82 (2015)
- [48] Van Der Maaten, L.: Accelerating t-sne using tree-based algorithms. *The journal of machine learning research* **15**(1), 3221–3245 (2014)
- [49] Saul, L.K., Roweis, S.T.: Think globally, fit locally: unsupervised learning of low dimensional manifolds. *Journal of machine learning research* **4**(Jun), 119–155 (2003)
- [50] Ge, S.S., Yang, Y., Lee, T.H.: Hand gesture recognition and tracking based on distributed locally linear embedding. *Image and Vision Computing* **26**(12), 1607–1620 (2008)
- [51] Pan, Y., Ge, S.S., Al Mamun, A.: Weighted locally linear embedding for dimension reduction. *Pattern Recognition* **42**(5), 798–811 (2009)
- [52] Zhou, X., Yang, C., Zhao, H., Yu, W.: Low-rank modeling and its applications in image analysis. *ACM Computing Surveys (CSUR)* **47**(2), 1–33 (2014)
- [53] Gu, S., Timofte, R.: A brief review of image denoising algorithms and beyond. *Inpainting and Denoising Challenges*, 1–21 (2019)
- [54] Haeffele, B., Young, E., Vidal, R.: Structured low-rank matrix factorization: Optimality, algorithm, and applications to image processing. In: *International Conference on Machine Learning*, pp. 2007–2015 (2014). PMLR
- [55] Ebiele, J., Ansah-Narh, T., Djokap, S., Proven-Adzri, E., Atemkeng, M.: Conventional machine learning based on feature engineering for detecting pneumonia from chest x-rays. In: *Conference of the South African Institute of Computer Scientists and Information Technologists 2020*, pp. 149–155 (2020)
- [56] Lee, J.-G., Jun, S., Cho, Y.-W., Lee, H., Kim, G.B., Seo, J.B., Kim, N.: Deep learning in medical imaging: general overview. *Korean journal of radiology* **18**(4), 570–584 (2017)
- [57] Müller, H., Michoux, N., Bandon, D., Geissbuhler, A.: A review of content-based image retrieval systems in medical applications—clinical benefits and future directions. *International journal of medical informatics* **73**(1), 1–23 (2004)

- [58] Razzak, M.I., Naz, S., Zaib, A.: Deep learning for medical image processing: Overview, challenges and the future. *Classification in BioApps: Automation of Decision Making*, 323–350 (2018)
- [59] Magrabi, F., Ong, M.-S., Runciman, W., Coiera, E.: Using fda reports to inform a classification for health information technology safety problems. *Journal of the American Medical Informatics Association* **19**(1), 45–53 (2012)
- [60] Shellock, F.G.: Magnetic resonance safety update 2002: implants and devices. *Journal of Magnetic Resonance Imaging: An Official Journal of the International Society for Magnetic Resonance in Medicine* **16**(5), 485–496 (2002)
- [61] Catana, C.: Motion correction options in pet/mri. In: *Seminars in Nuclear Medicine*, vol. 45, pp. 212–223 (2015). Elsevier
- [62] Wang, Q., Chen, Y., Zhang, N., Gu, Y.: Medical image inpainting with edge and structure priors. *Measurement* **185**, 110027 (2021)
- [63] Armanious, K., Kumar, V., Abdulatif, S., Hepp, T., Gatidis, S., Yang, B.: ipa-medgan: Inpainting of arbitrary regions in medical imaging. In: *2020 IEEE International Conference on Image Processing (ICIP)*, pp. 3005–3009 (2020). IEEE
- [64] Li, J., He, F., Zhang, L., Du, B., Tao, D.: Progressive reconstruction of visual structure for image inpainting. In: *Proceedings of the IEEE/CVF International Conference on Computer Vision*, pp. 5962–5971 (2019)
- [65] Sweeney, K.T., Ward, T.E., McLoone, S.F.: Artifact removal in physiological signals—practices and possibilities. *IEEE transactions on information technology in biomedicine* **16**(3), 488–500 (2012)
- [66] Singh, B.N., Tiwari, A.K.: Optimal selection of wavelet basis function applied to ecg signal denoising. *Digital signal processing* **16**(3), 275–287 (2006)
- [67] Meng, C., Zelezniak, O.A., Thallinger, G.G., Kuster, B., Gholami, A.M., Culhane, A.C.: Dimension reduction techniques for the integrative analysis of multi-omics data. *Briefings in bioinformatics* **17**(4), 628–641 (2016)
- [68] Misra, B.B., Langefeld, C., Olivier, M., Cox, L.A.: Integrated omics: tools, advances and future approaches. *Journal of molecular endocrinology* **62**(1), 21–45 (2019)
- [69] Hao, M., Bryant, S.H., Wang, Y.: A new chemoinformatics approach with

improved strategies for effective predictions of potential drugs. *Journal of cheminformatics* **10**(1), 1–9 (2018)

[70] T Devinyak, O., B Lesyk, R.: 5-year trends in qsar and its machine learning methods. *Current Computer-Aided Drug Design* **12**(4), 265–271 (2016)

[71] He, K., Zhang, X., Xu, D., Gong, J., Xie, L.: Fidelity-driven optimization reconstruction and details preserving guided fusion for multi-modality medical image. *IEEE Transactions on Multimedia* (2022)

[72] Liu, S., Zhang, T., Li, H., Zhao, J., Li, H.: Medical image fusion based on nuclear norm minimization. *International Journal of Imaging Systems and Technology* **25**(4), 310–316 (2015)

[73] Zhong, L., Lin, L., Lu, Z., Wu, Y., Lu, Z., Huang, M., Yang, W., Feng, Q.: Predict ct image from mri data using knn-regression with learned local descriptors. In: 2016 IEEE 13th International Symposium on Biomedical Imaging (ISBI), pp. 743–746 (2016). IEEE

[74] Huang, C., Ding, X., Fang, C., Wen, D.: Robust image restoration via adaptive low-rank approximation and joint kernel regression. *IEEE Transactions on Image Processing* **23**(12), 5284–5297 (2014)

[75] Lu, H., Wei, J., Wang, L., Liu, P., Liu, Q., Wang, Y., Deng, X.: Reference information based remote sensing image reconstruction with generalized nonconvex low-rank approximation. *Remote Sensing* **8**(6), 499 (2016)

[76] Lu, H., Liu, Q., Zhang, M., Wang, Y., Deng, X.: Gradient-based low rank method and its application in image inpainting. *Multimedia Tools and Applications* **77**, 5969–5993 (2018)

[77] Oseledets, I.V., Tyrtyshnikov, E.E.: Breaking the curse of dimensionality, or how to use svd in many dimensions. *SIAM Journal on Scientific Computing* **31**(5), 3744–3759 (2009)

[78] Hastie, T., Mazumder, R., Lee, J.D., Zadeh, R.: Matrix completion and low-rank svd via fast alternating least squares. *The Journal of Machine Learning Research* **16**(1), 3367–3402 (2015)

[79] Holmes, M., Gray, A., Isbell, C.: Fast svd for large-scale matrices. In: Workshop on Efficient Machine Learning at NIPS, vol. 58, pp. 249–252 (2007)

[80] Mamat, N.J.Z., Daniel, J.K.: Statistical analyses on time complexity and rank consistency between singular value decomposition and the duality approach in ahp: A case study of faculty member selection. *Mathematical*

and Computer Modelling **46**(7-8), 1099–1106 (2007)

- [81] Brand, M.: Fast low-rank modifications of the thin singular value decomposition. *Linear algebra and its applications* **415**(1), 20–30 (2006)
- [82] Roughgarden, T., Valiant, G.: Cs168: The modern algorithmic toolbox lecture# 9: The singular value decomposition (svd) and low-rank matrix approximations. [Online], <http://theory.stanford.edu/~tim/s15/1/19.pdf>. Accessed:[29 June 2019] (2015)
- [83] Atemkeng, M., Perkins, S., Seck, E., Makhathini, S., Smirnov, O., Bester, L., Hugo, B.: Lossy compression of large-scale radio interferometric data. *arXiv preprint arXiv:2304.07050* (2023)
- [84] Halko, N., Martinsson, P.-G., Tropp, J.A.: Finding structure with randomness: Probabilistic algorithms for constructing approximate matrix decompositions. *SIAM review* **53**(2), 217–288 (2011)
- [85] Burca, V.S.: Fast monte carlo algorithms for computing a low-rank approximation to a matrix (2014)
- [86] Lee, J., Kim, S., Lebanon, G., Singer, Y.: Local low-rank matrix approximation. In: *International Conference on Machine Learning*, pp. 82–90 (2013). PMLR
- [87] Liu, H., Jing, L., Qian, Y., Yu, J.: Adaptive local low-rank matrix approximation for recommendation. *ACM Transactions on Information Systems (TOIS)* **37**(4), 1–34 (2019)
- [88] Guo, Q., Gao, S., Zhang, X., Yin, Y., Zhang, C.: Patch-based image inpainting via two-stage low rank approximation. *IEEE transactions on visualization and computer graphics* **24**(6), 2023–2036 (2017)
- [89] Dib, E., Le Pendu, M., Jiang, X., Guillemot, C.: Local low rank approximation with a parametric disparity model for light field compression. *IEEE Transactions on Image Processing* **29**, 9641–9653 (2020)
- [90] Lee, J., Kim, S., Lebanon, G., Singer, Y., Bengio, S.: Llorma: Local low-rank matrix approximation (2016)
- [91] Dhawan, A.P.: *Medical Image Analysis*. John Wiley & Sons, ??? (2011)
- [92] Saladi, S., Amutha Prabha, N.: Analysis of denoising filters on mri brain images. *International Journal of Imaging Systems and Technology* **27**(3), 201–208 (2017)
- [93] Pandey, M., Bhatia, M., Bansal, A.: An anatomization of noise removal techniques on medical images. In: *2016 International Conference on*

Innovation and Challenges in Cyber Security (ICICCS-INBUSH), pp. 224–229 (2016). IEEE

- [94] Lyra-Leite, D.M., da Costa, J.P.C.L., de Carvalho, J.L.A.: Improved mri reconstruction and denoising using svd-based low-rank approximation. In: 2012 Workshop on Engineering Applications, pp. 1–6 (2012). IEEE
- [95] McGivney, D.F., Pierre, E., Ma, D., Jiang, Y., Saybasili, H., Gulani, V., Griswold, M.A.: Svd compression for magnetic resonance fingerprinting in the time domain. *IEEE transactions on medical imaging* **33**(12), 2311–2322 (2014)
- [96] Fang, R., Huang, J., Luh, W.-M.: A spatio-temporal low-rank total variation approach for denoising arterial spin labeling mri data. In: 2015 IEEE 12th International Symposium on Biomedical Imaging (ISBI), pp. 498–502 (2015). IEEE
- [97] Yang, M., Ma, D., Jiang, Y., Hamilton, J., Seiberlich, N., Griswold, M.A., McGivney, D.: Low rank approximation methods for mr fingerprinting with large scale dictionaries. *Magnetic resonance in medicine* **79**(4), 2392–2400 (2018)
- [98] Kopriva, I., Shi, F., Lai, M., Štanfel, M., Chen, H., Chen, X.: Low tensor train and low multilinear rank approximations of 3d tensors for compression and de-speckling of optical coherence tomography images. *Physics in Medicine & Biology* **68**(12), 125002 (2023)
- [99] Doukas, C., Maglogiannis, I.: Region of interest coding techniques for medical image compression. *IEEE Engineering in medicine and Biology Magazine* **26**(5), 29–35 (2007)
- [100] Wang, J., Huang, K.: Medical image compression by using three-dimensional wavelet transformation. *IEEE Transactions on Medical Imaging* **15**(4), 547–554 (1996)
- [101] Zukoski, M.J., Boult, T., Iyriboz, T.: A novel approach to medical image compression. *International journal of bioinformatics research and applications* **2**(1), 89–103 (2006)
- [102] Assländer, J., Cloos, M.A., Knoll, F., Sodickson, D.K., Hennig, J., Lattanzi, R.: Low rank alternating direction method of multipliers reconstruction for mr fingerprinting. *Magnetic resonance in medicine* **79**(1), 83–96 (2018)
- [103] Peng, X., Ying, L., Liu, Y., Yuan, J., Liu, X., Liang, D.: Accelerated exponential parameterization of t2 relaxation with model-driven low rank and sparsity priors (morasa). *Magnetic resonance in medicine*

76(6), 1865–1878 (2016)

- [104] Ulas, C., Gómez, P.A., Sperl, J.I., Preibisch, C., Menze, B.H.: Spatio-temporal mri reconstruction by enforcing local and global regularity via dynamic total variation and nuclear norm minimization. In: 2016 IEEE 13th International Symposium on Biomedical Imaging (ISBI), pp. 306–309 (2016). IEEE
- [105] Xu, F., Han, J., Wang, Y., Chen, M., Chen, Y., He, G., Hu, Y.: Dynamic magnetic resonance imaging via nonconvex low-rank matrix approximation. *IEEE Access* **5**, 1958–1966 (2017)
- [106] Li, X.P., Liu, Q., So, H.C.: Rank-one matrix approximation with l_p -norm for image inpainting. *IEEE Signal Processing Letters* **27**, 680–684 (2020)
- [107] Friedland, S., Niknejad, A., Kaveh, M., Zare, H.: An algorithm for missing value estimation for dna microarray data. In: 2006 IEEE International Conference on Acoustics Speech and Signal Processing Proceedings, vol. 2, p. (2006). IEEE
- [108] Liu, X., Jing, X.-Y., Tang, G., Wu, F., Dong, X.: Low-rank tensor completion for visual data recovery via the tensor train rank-1 decomposition. *IET Image Processing* **14**(1), 114–124 (2020)
- [109] Yi, Z., Liu, Y., Zhao, Y., Xiao, L., Leong, A.T., Feng, Y., Chen, F., Wu, E.X.: Joint calibrationless reconstruction of highly undersampled multicontrast mr datasets using a low-rank hankel tensor completion framework. *Magnetic Resonance in Medicine* **85**(6), 3256–3271 (2021)
- [110] Cheng, E., Pang, Y., Zhu, Y., Yu, J., Ling, H.: Curvilinear structure tracking by low rank tensor approximation with model propagation. In: Proceedings of the IEEE Conference on Computer Vision and Pattern Recognition, pp. 3057–3064 (2014)
- [111] Jia, H., Chen, X., Han, Z., Liu, B., Wen, T., Tang, Y.: Nonconvex nonlocal tucker decomposition for 3d medical image super-resolution. *Frontiers in Neuroinformatics* **16**, 880301 (2022)
- [112] Kishore Kumar, N., Schneider, J.: Literature survey on low rank approximation of matrices. *Linear and Multilinear Algebra* **65**(11), 2212–2244 (2017)
- [113] Nguyen, N.H., Do, T.T., Tran, T.D.: A fast and efficient algorithm for low-rank approximation of a matrix. In: Proceedings of the Forty-first Annual ACM Symposium on Theory of Computing, pp. 215–224 (2009)
- [114] Achlioptas, D., McSherry, F.: Fast computation of low-rank matrix

approximations. *Journal of the ACM (JACM)* **54**(2), 9 (2007)

[115] Chu, M.T., Funderlic, R.E., Plemmons, R.J.: Structured low rank approximation. *Linear algebra and its applications* **366**, 157–172 (2003)

[116] Liberty, E., Woolfe, F., Martinsson, P.-G., Rokhlin, V., Tygert, M.: Randomized algorithms for the low-rank approximation of matrices. *Proceedings of the National Academy of Sciences* **104**(51), 20167–20172 (2007)

[117] Chen, L.-C., Papandreou, G., Kokkinos, I., Murphy, K., Yuille, A.L.: Deeplab: Semantic image segmentation with deep convolutional nets, atrous convolution, and fully connected crfs. *IEEE transactions on pattern analysis and machine intelligence* **40**(4), 834–848 (2017)

[118] Uman, L.S.: Systematic reviews and meta-analyses. *Journal of the Canadian Academy of Child and Adolescent Psychiatry* **20**(1), 57 (2011)

[119] Chung, J., Chung, M.: Optimal regularized inverse matrices for inverse problems. *SIAM Journal on Matrix Analysis and Applications* **38**(2), 458–477 (2017)

[120] Mahoney, M.W., Maggioni, M., Drineas, P.: Tensor-cur decompositions for tensor-based data. In: *Proceedings of the 12th ACM SIGKDD International Conference on Knowledge Discovery and Data Mining*, pp. 327–336 (2006)

[121] Ding, Q., Niu, T., Zhang, X., Long, Y.: Image-domain multimaterial decomposition for dual-energy ct based on prior information of material images. *Medical physics* **45**(8), 3614–3626 (2018)

[122] Zhen, X., Yu, M., Islam, A., Bhaduri, M., Chan, I., Li, S.: Descriptor learning via supervised manifold regularization for multioutput regression. *IEEE transactions on neural networks and learning systems* **28**(9), 2035–2047 (2016)

[123] Fu, Y., Dong, W.: 3d magnetic resonance image denoising using low-rank tensor approximation. *Neurocomputing* **195**, 30–39 (2016)

[124] Chen, Z., Fu, Y., Xiang, Y., Zhu, Y.: A novel mr image denoising via lrma and nlss. *Signal Processing* **185**, 108109 (2021)

[125] Xia, Y., Gao, Q., Cheng, N., Lu, Y., Zhang, D., Ye, Q.: Denoising 3-d magnitude magnetic resonance images based on weighted nuclear norm minimization. *Biomedical Signal Processing and Control* **34**, 183–194 (2017)

- [126] Khaleel, H.S., Sagheer, S.V.M., Baburaj, M., George, S.N.: Denoising of rician corrupted 3d magnetic resonance images using tensor-svd. *Biomedical Signal Processing and Control* **44**, 82–95 (2018)
- [127] Zhai, L., Fu, S., Lv, H., Zhang, C., Wang, F.: Weighted schatten p-norm minimization for 3d magnetic resonance images denoising. *Brain Research Bulletin* **142**, 270–280 (2018)
- [128] Mandava, S., Keerthivasan, M.B., Li, Z., Martin, D.R., Altbach, M.I., Bilgin, A.: Accelerated mr parameter mapping with a union of local subspaces constraint. *Magnetic Resonance in Medicine* **80**(6), 2744–2758 (2018)
- [129] Lv, H., Wang, R.: Denoising 3d magnetic resonance images based on low-rank tensor approximation with adaptive multirank estimation. *IEEE Access* **7**, 85995–86003 (2019)
- [130] Wang, L., Xiao, D., Hou, W.S., Wu, X.Y., Chen, L.: A modified higher-order singular value decomposition framework with adaptive multilinear tensor rank approximation for three-dimensional magnetic resonance rician noise removal. *Frontiers in Oncology* **10**, 1640 (2020)
- [131] Chen, Z., Zhou, Z., Adnan, S.: Joint low-rank prior and difference of gaussian filter for magnetic resonance image denoising. *Medical & Biological Engineering & Computing* **59**, 607–620 (2021)
- [132] Zhang, Y., Kang, R., Peng, X., Wang, J., Zhu, J., Peng, J., Liu, H.: Image denoising via structure-constrained low-rank approximation. *Neural Computing and Applications* **32**, 12575–12590 (2020)
- [133] Zhao, Y., Yi, Z., Xiao, L., Lau, V., Liu, Y., Zhang, Z., Guo, H., Leong, A.T., Wu, E.X.: Joint denoising of diffusion-weighted images via structured low-rank patch matrix approximation. *Magnetic Resonance in Medicine* **88**(6), 2461–2474 (2022)
- [134] He, J., Gao, P., Zheng, X., Zhou, Y., He, H.: Denoising 3d magnetic resonance images based on weighted tensor nuclear norm minimization using balanced nonlocal patch tensors. *Biomedical Signal Processing and Control* **74**, 103524 (2022)
- [135] Lei, Y., Xu, D., Zhou, Z., Wang, T., Dong, X., Liu, T., Dhabaan, A., Curran, W.J., Yang, X.: A denoising algorithm for ct image using low-rank sparse coding. In: *Medical Imaging 2018: Image Processing*, vol. 10574, pp. 434–440 (2018). SPIE
- [136] Sagheer, S.V.M., George, S.N.: Denoising of low-dose ct images via low-rank tensor modeling and total variation regularization. *Artificial*

intelligence in medicine **94**, 1–17 (2019)

- [137] Shen, Y., Sun, S., Xu, F., Liu, Y., Yin, X., Zhou, X.: Ct image reconstruction via nonlocal low-rank regularization and data-driven tight frame. *Symmetry* **13**(10), 1873 (2021)
- [138] Hariharan, S.G., Kaethner, C., Strobel, N., Kowarschik, M., DiNitto, J., Albarqouni, S., Fahrig, R., Navab, N.: Preliminary results of dsa denoising based on a weighted low-rank approach using an advanced neurovascular replication system. *International Journal of Computer Assisted Radiology and Surgery* **14**, 1117–1126 (2019)
- [139] Hariharan, S.G., Strobel, N., Kaethner, C., Kowarschik, M., Demirci, S., Albarqouni, S., Fahrig, R., Navab, N.: A photon recycling approach to the denoising of ultra-low dose x-ray sequences. *International journal of computer assisted radiology and surgery* **13**, 847–854 (2018)
- [140] Sagheer, S.V.M., George, S.N.: Ultrasound image despeckling using low rank matrix approximation approach. *Biomedical Signal Processing and Control* **38**, 236–249 (2017)
- [141] Sagheer, S.V.M., George, S.N., Kurien, S.K.: Despeckling of 3d ultrasound image using tensor low rank approximation. *Biomedical Signal Processing and Control* **54**, 101595 (2019)
- [142] Yang, H., Zhang, H., Luo, Y., Lu, J., Lu, J.: Ultrasound image restoration using weighted nuclear norm minimization. In: 2020 25th International Conference on Pattern Recognition (ICPR), pp. 5391–5397 (2021). IEEE
- [143] Xie, N., Chen, Y., Liu, H.: 3d tensor based nonlocal low rank approximation in dynamic pet reconstruction. *Sensors* **19**(23), 5299 (2019)
- [144] Yang, Z., Sheng, Y., Chai, L., Yi, L.: Pet image denoising based on non-local low rank matrix approximation. In: 2020 Chinese Control And Decision Conference (CCDC), pp. 5039–5044 (2020). IEEE
- [145] He, Y., Jiao, W., Shi, Y., Lian, J., Zhao, B., Zou, W., Zhu, Y., Zheng, Y.: Segmenting diabetic retinopathy lesions in multispectral images using low-dimensional spatial-spectral matrix representation. *IEEE journal of biomedical and health informatics* **24**(2), 493–502 (2019)
- [146] Ren, X., Zheng, Y., Zhao, Y., Luo, C., Wang, H., Lian, J., He, Y.: Drusen segmentation from retinal images via supervised feature learning. *IEEE Access* **6**, 2952–2961 (2017)
- [147] Yang, W., Zhong, L., Chen, Y., Lin, L., Lu, Z., Liu, S., Wu, Y., Feng, Q., Chen, W.: Predicting ct image from mri data through feature matching

with learned nonlinear local descriptors. *IEEE transactions on medical imaging* **37**(4), 977–987 (2018)

[148] Liu, H., Guo, Q., Wang, G., Gupta, B.B., Zhang, C.: Medical image resolution enhancement for healthcare using nonlocal self-similarity and low-rank prior. *Multimedia Tools and Applications* **78**, 9033–9050 (2019)

[149] Yousefi, B., Sharifipour, H.M., Mal dague, X.P.: A diagnostic biomarker for breast cancer screening via hilbert embedded deep low-rank matrix approximation. *IEEE Transactions on Instrumentation and Measurement* **70**, 1–9 (2021)

[150] Ji, L., Guo, Q., Zhang, M.: Medical image denoising based on biquadratic polynomial with minimum error constraints and low-rank approximation. *IEEE Access* **8**, 84950–84960 (2020)

[151] Fix, E., Hodges, J.L.: Discriminatory analysis. nonparametric discrimination: Consistency properties. *International Statistical Review/Revue Internationale de Statistique* **57**(3), 238–247 (1989)

[152] MacQueen, J., *et al.*: Some methods for classification and analysis of multivariate observations. In: *Proceedings of the Fifth Berkeley Symposium on Mathematical Statistics and Probability*, vol. 1, pp. 281–297 (1967). Oakland, CA, USA

[153] Deisenroth, M.P., Faisal, A.A., Ong, C.S.: *Mathematics for Machine Learning*. Cambridge University Press, ??? (2020)

[154] Zhou, D., Weston, J., Gretton, A., Bousquet, O., Schölkopf, B.: Ranking on data manifolds. *Advances in neural information processing systems* **16** (2003)

[155] Barnes, C., Shechtman, E., Goldman, D.B., Finkelstein, A.: The generalized patchmatch correspondence algorithm. In: *Computer Vision–ECCV 2010: 11th European Conference on Computer Vision, Heraklion, Crete, Greece, September 5–11, 2010, Proceedings, Part III* 11, pp. 29–43 (2010). Springer

[156] Mairal, J., Bach, F., Ponce, J., Sapiro, G., Zisserman, A.: Non-local sparse models for image restoration. In: *2009 IEEE 12th International Conference on Computer Vision*, pp. 2272–2279 (2009). IEEE

[157] Bishop, C.M., Nasrabadi, N.M.: *Pattern Recognition and Machine Learning* vol. 4. Springer, ??? (2006)

[158] Goodfellow, I., Bengio, Y., Courville, A.: *Deep Learning*. MIT press, ???

(2016)

- [159] Roberts, D.A., Yaida, S., Hanin, B.: The Principles of Deep Learning Theory. Cambridge University Press Cambridge, MA, USA, ??? (2022)
- [160] Gray, R.M., Gray, R.: Probability, Random Processes, and Ergodic Properties vol. 1. Springer, ??? (2009)
- [161] Cohn, D.L.: Measure Theory vol. 5. Springer, ??? (2013)
- [162] Halmos, P.R.: Measure Theory vol. 18. Springer, ??? (2013)
- [163] Hamming, R.W.: Error detecting and error correcting codes. *The Bell system technical journal* **29**(2), 147–160 (1950)
- [164] Laaksonen, J., Oja, E.: Classification with learning k-nearest neighbors. In: Proceedings of International Conference on Neural Networks (ICNN'96), vol. 3, pp. 1480–1483 (1996). IEEE
- [165] Khalid, N.E.A., Ibrahim, S., Haniff, P.: Mri brain abnormalities segmentation using k-nearest neighbors(k-nn). *International Journal on Computer Science and Engineering* **3**(2), 980–990 (2011)
- [166] Hu, L.-Y., Huang, M.-W., Ke, S.-W., Tsai, C.-F.: The distance function effect on k-nearest neighbor classification for medical datasets. *SpringerPlus* **5**(1), 1–9 (2016)
- [167] Mack, Y.-P.: Local properties of k-nn regression estimates. *SIAM Journal on Algebraic Discrete Methods* **2**(3), 311–323 (1981)
- [168] Sarker, I.H.: Machine learning: Algorithms, real-world applications and research directions. *SN computer science* **2**(3), 160 (2021)
- [169] Bi, X., Li, S., Xiao, B., Li, Y., Wang, G., Ma, X.: Computer aided alzheimer's disease diagnosis by an unsupervised deep learning technology. *Neurocomputing* **392**, 296–304 (2020)
- [170] Chander, B., Gopalakrishnan, K.: Data clustering using unsupervised machine learning. In: *Statistical Modeling in Machine Learning*, pp. 179–204. Elsevier, ??? (2023)
- [171] Guo, Y., Gao, Y., Shen, D.: Deformable mr prostate segmentation via deep feature learning and sparse patch matching. *IEEE transactions on medical imaging* **35**(4), 1077–1089 (2015)
- [172] Cordier, N., Delingette, H., Ayache, N.: A patch-based approach for the segmentation of pathologies: application to glioma labelling. *IEEE transactions on medical imaging* **35**(4), 1066–1076 (2015)

- [173] Mechrez, R., Goldberger, J., Greenspan, H.: Patch-based segmentation with spatial consistency: application to ms lesions in brain mri. *Journal of Biomedical Imaging* **2016**, 3–3 (2016)
- [174] Wu, G., Wang, Q., Jia, H., Shen, D.: Feature-based groupwise registration by hierarchical anatomical correspondence detection. *Human Brain Mapping* **33**(2), 253–271 (2012)
- [175] Tong, T., Wolz, R., Coupe, P., Hajnal, J.V., Rueckert, D.: Discriminative dictionary learning for abdominal multi-organ segmentation. *Medical Image Analysis* **23**(1), 92–104 (2015)
- [176] Sotiras, A., Davatzikos, C., Paragios, N.: Deformable medical image registration: A survey. *IEEE Transactions on Medical Imaging* **32**(7), 1153–1190 (2013)
- [177] Ledesma-Carbayo, M.J., Kybic, J., Desco, M., Santos, A., Suhling, M., Hunziker, P., Unser, M.: Spatio-temporal nonrigid registration for ultrasound cardiac motion estimation. *IEEE Transactions on Medical Imaging* **24**(9), 1113–1126 (2005)
- [178] Wall, M.E., Rechtsteiner, A., Rocha, L.M.: Singular value decomposition and principal component analysis. In: *A Practical Approach to Microarray Data Analysis*, pp. 91–109. Springer, ??? (2003)
- [179] Stewart, G.W.: On the early history of the singular value decomposition. *SIAM review* **35**(4), 551–566 (1993)
- [180] Klema, V., Laub, A.: The singular value decomposition: Its computation and some applications. *IEEE Transactions on automatic control* **25**(2), 164–176 (1980)
- [181] Aishwarya, K., Ramesh, R., Sobarad, P.M., Singh, V.: Lossy image compression using svd coding algorithm. In: *2016 International Conference on Wireless Communications, Signal Processing and Networking (WiSPNET)*, pp. 1384–1389 (2016). IEEE
- [182] Van Loan, C.F.: Generalizing the singular value decomposition. *SIAM Journal on numerical Analysis* **13**(1), 76–83 (1976)
- [183] Paulsen, V.I., Power, S.C., Smith, R.R.: Schur products and matrix completions. *Journal of functional analysis* **85**(1), 151–178 (1989)
- [184] Chen, H.-H.: Weighted-svd: Matrix factorization with weights on the latent factors. *arXiv preprint arXiv:1710.00482* (2017)
- [185] Mahoney, M.W., *et al.*: Randomized algorithms for matrices and data.

Foundations and Trends® in Machine Learning **3**(2), 123–224 (2011)

[186] Gower, R.M., Richtárik, P.: Randomized iterative methods for linear systems. SIAM Journal on Matrix Analysis and Applications **36**(4), 1660–1690 (2015)

[187] Brunton, S.L., Kutz, J.N.: Data-driven Science and Engineering: Machine Learning, Dynamical Systems, and Control. Cambridge University Press, ??? (2022)

[188] Singh, G., Gupta, S., Lease, M., Dawson, C.: Range-net: A high precision streaming svd for big data applications. arXiv preprint arXiv:2010.14226 (2020)

[189] Kilmer, M.E., Horesh, L., Avron, H., Newman, E.: Tensor-tensor algebra for optimal representation and compression of multiway data. Proceedings of the National Academy of Sciences **118**(28), 2015851118 (2021)

[190] Wang, M., Hong, D., Han, Z., Li, J., Yao, J., Gao, L., Zhang, B., Chanussot, J.: Tensor decompositions for hyperspectral data processing in remote sensing: A comprehensive review. IEEE Geoscience and Remote Sensing Magazine (2023)

[191] Van Der Maaten, L., Postma, E., Van den Herik, J., et al.: Dimensionality reduction: a comparative. J Mach Learn Res **10**(66–71) (2009)

[192] Li, X., Wang, S., Cai, Y.: Tutorial: Complexity analysis of singular value decomposition and its variants. arXiv preprint arXiv:1906.12085 (2019)

[193] Mallat, S.: Understanding deep convolutional networks. Philosophical Transactions of the Royal Society A: Mathematical, Physical and Engineering Sciences **374**(2065), 20150203 (2016)

[194] Mozaffari, M., Markopoulos, P.P.: Robust barron-loss tucker tensor decomposition. In: 2021 55th Asilomar Conference on Signals, Systems, and Computers, pp. 1651–1655 (2021). IEEE

[195] Yeong, D.J., Velasco-Hernandez, G., Barry, J., Walsh, J.: Sensor and sensor fusion technology in autonomous vehicles: A review. Sensors **21**(6), 2140 (2021)

[196] Miglani, A., Kumar, N.: Deep learning models for traffic flow prediction in autonomous vehicles: A review, solutions, and challenges. Vehicular Communications **20**, 100184 (2019)

[197] Gupta, A., Anpalagan, A., Guan, L., Khwaja, A.S.: Deep learning

for object detection and scene perception in self-driving cars: Survey, challenges, and open issues. *Array* **10**, 100057 (2021)

[198] Nandwani, P., Verma, R.: A review on sentiment analysis and emotion detection from text. *Social Network Analysis and Mining* **11**(1), 81 (2021)

[199] Koroteev, M.: Bert: a review of applications in natural language processing and understanding. *arXiv preprint arXiv:2103.11943* (2021)

[200] Ekman, M.: Learning Deep Learning: Theory and Practice of Neural Networks, Computer Vision, Natural Language Processing, and Transformers Using TensorFlow. Addison-Wesley Professional, ??? (2021)

[201] Romero, C., Ventura, S.: Data mining in education. *Wiley Interdisciplinary Reviews: Data mining and knowledge discovery* **3**(1), 12–27 (2013)

[202] Alzubaidi, L., Zhang, J., Humaidi, A.J., Al-Dujaili, A., Duan, Y., Al-Shamma, O., Santamaría, J., Fadhel, M.A., Al-Amidie, M., Farhan, L.: Review of deep learning: Concepts, cnn architectures, challenges, applications, future directions. *Journal of big Data* **8**, 1–74 (2021)

[203] Youssef, F., Houda, B.: Comparative study of end-to-end deep learning methods for self-driving car. *International Journal of Intelligent Systems and Applications* **12**, 15–27 (2020)

[204] Otter, D.W., Medina, J.R., Kalita, J.K.: A survey of the usages of deep learning for natural language processing. *IEEE transactions on neural networks and learning systems* **32**(2), 604–624 (2020)

[205] Demner-Fushman, D., Chapman, W.W., McDonald, C.J.: What can natural language processing do for clinical decision support? *Journal of biomedical informatics* **42**(5), 760–772 (2009)

[206] Velupillai, S., Suominen, H., Liakata, M., Roberts, A., Shah, A.D., Morley, K., Osborn, D., Hayes, J., Stewart, R., Downs, J., *et al.*: Using clinical natural language processing for health outcomes research: overview and actionable suggestions for future advances. *Journal of biomedical informatics* **88**, 11–19 (2018)

[207] Habeeb, R.A.A., Nasaruddin, F., Gani, A., Hashem, I.A.T., Ahmed, E., Imran, M.: Real-time big data processing for anomaly detection: A survey. *International Journal of Information Management* **45**, 289–307 (2019)

[208] Sagiroglu, S., Sinanc, D.: Big data: A review. In: 2013 International

Conference on Collaboration Technologies and Systems (CTS), pp. 42–47 (2013). IEEE

- [209] Ma, L., Sun, B.: Machine learning and ai in marketing—connecting computing power to human insights. *International Journal of Research in Marketing* **37**(3), 481–504 (2020)
- [210] Johnson, K.B., Wei, W.-Q., Weeraratne, D., Frisse, M.E., Misulis, K., Rhee, K., Zhao, J., Snowdon, J.L.: Precision medicine, ai, and the future of personalized health care. *Clinical and translational science* **14**(1), 86–93 (2021)
- [211] Wang, Y., Kung, L., Byrd, T.A.: Big data analytics: Understanding its capabilities and potential benefits for healthcare organizations. *Technological forecasting and social change* **126**, 3–13 (2018)
- [212] Tayefi, M., Ngo, P., Chomutare, T., Dalianis, H., Salvi, E., Budrionis, A., Godtliebsen, F.: Challenges and opportunities beyond structured data in analysis of electronic health records. *Wiley Interdisciplinary Reviews: Computational Statistics* **13**(6), 1549 (2021)
- [213] Zimmerman, M., McGlinchey, J., Chelminski, I., Young, D.: Diagnostic co-morbidity in 2300 psychiatric out-patients presenting for treatment evaluated with a semi-structured diagnostic interview. *Psychological Medicine* **38**(2), 199–210 (2008)
- [214] Kong, Q., Cao, Y., Iqbal, T., Wang, Y., Wang, W., Plumbley, M.D.: Panns: Large-scale pretrained audio neural networks for audio pattern recognition. *IEEE/ACM Transactions on Audio, Speech, and Language Processing* **28**, 2880–2894 (2020)
- [215] Rusu, O., Halcu, I., Grigoriu, O., Neculoiu, G., Sandulescu, V., Marinescu, M., Marinescu, V.: Converting unstructured and semi-structured data into knowledge. In: 2013 11th RoEduNet International Conference, pp. 1–4 (2013). IEEE
- [216] Hou, F., Lei, W., Li, S., Xi, J., Xu, M., Luo, J.: Improved mask r-cnn with distance guided intersection over union for gpr signature detection and segmentation. *Automation in Construction* **121**, 103414 (2021)